

# Long-term stochastic model predictive control for the energy management of hybrid electric vehicles using Pontryagin's minimum principle and scenario-based optimization

## Journal Article

**Author(s):**

Ritter, Andreas ; Widmer, Fabio ; Duhr, Pol ; Onder, Christopher H.

**Publication date:**

2022-09-15

**Permanent link:**

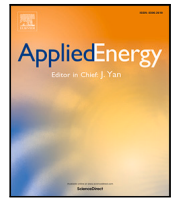
<https://doi.org/https://doi.org/10.3929/ethz-b-000553595>

**Rights / license:**

[Creative Commons Attribution 4.0 International](#)

**Originally published in:**

Applied Energy 322, <https://doi.org/10.1016/j.apenergy.2022.119192>

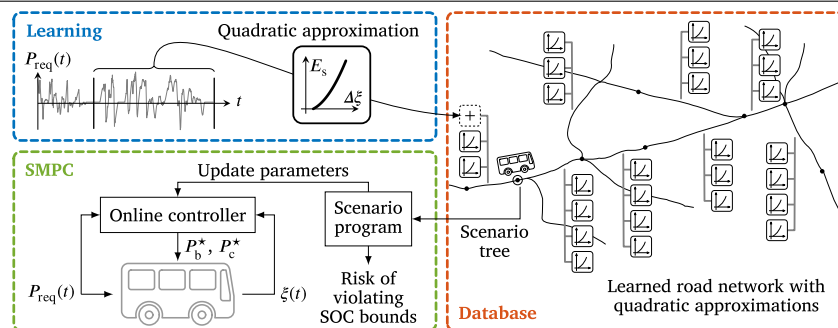


# Long-term stochastic model predictive control for the energy management of hybrid electric vehicles using Pontryagin's minimum principle and scenario-based optimization

Andreas Ritter\*, Fabio Widmer, Pol Duhr, Christopher H. Onder

Institute for Dynamic Systems and Control, ETH Zürich, 8092 Zürich, Switzerland

## GRAPHICAL ABSTRACT



## ARTICLE INFO

### Keywords:

Hybrid electric vehicles  
Energy management system  
Model predictive control  
Scenario optimization

## ABSTRACT

This paper presents a new approach to efficiently integrate long prediction horizons subject to uncertainty into a stochastic model predictive control (MPC) framework for the energy management of hybrid electric vehicles. By exploiting Pontryagin's minimum principle, we show that the energy supply required to obtain a certain change in the state of charge (SOC) of the battery can be approximated using a quadratic equation. The parameters of these mappings depend on the power request imposed by the driving mission and thus allow to compress the time-resolved power profile into only three scalar variables. Having a driving mission divided into several segments of arbitrary length, the corresponding sequence of quadratic approximations allows to reformulate the original energy management problem as a quadratic program, which offers an efficient way to include a large number of future scenarios. The resulting scenario-based stochastic MPC approach prevents SOC boundary violations with a certain probability, which can be controlled by the number of scenarios considered. To validate the quadratic approximation, we study two numerical examples using two different vehicles, a series hybrid electric passenger car and a battery-assisted trolley bus. Finally, a case study based on the operation of the latter is provided, which demonstrates the expected behavior and the real-time capability of the stochastic MPC approach. While the SOC is maintained in predefined boundaries with high probability, the required energy supply is only increased by 1.41% compared to the non-causal optimum.

\* Corresponding author.

E-mail addresses: [anritter@idsc.mavt.ethz.ch](mailto:anritter@idsc.mavt.ethz.ch) (A. Ritter), [fawidmer@idsc.mavt.ethz.ch](mailto:fawidmer@idsc.mavt.ethz.ch) (F. Widmer), [pduhr@idsc.mavt.ethz.ch](mailto:pduhr@idsc.mavt.ethz.ch) (P. Duhr), [onder@idsc.mavt.ethz.ch](mailto:onder@idsc.mavt.ethz.ch) (C.H. Onder).

<https://doi.org/10.1016/j.apenergy.2022.119192>

Received 29 July 2021; Received in revised form 20 January 2022; Accepted 21 April 2022

Available online 18 June 2022

0306-2619/© 2022 The Authors. Published by Elsevier Ltd. This is an open access article under the CC BY license (<http://creativecommons.org/licenses/by/4.0/>).

## 1. Introduction

### 1.1. Context and motivation

Although overall greenhouse gas emissions in the European Union have been declining in recent years, preliminary estimates show an increasing trend in the emissions of the transport sector in 2018 and 2019 [1]. Consequently, the relative influence of the transport sector on the total emissions has increased. This demands further actions in order to achieve the goal of zero net greenhouse gas emissions in 2050 set by the European Green Deal [2], especially in road transport, the largest contributor to transport emissions with around 71% in 2018 [1].

One approach pursued in this context is to increase the energy efficiency of the vehicle fleet, which is mainly achieved with its electrification using hybrid electric vehicles (HEVs) and battery electric vehicles (BEVs). However, both technologies have certain shortcomings. While the former is still relying on fuels as the main power source, the latter is afflicted by what is known as range anxiety [3], where drivers are concerned about the travel distances reachable. In both cases, the drawbacks can be mitigated by using predictive information about the upcoming driving operation: For HEVs, predictions of the future power request allow to minimize the fuel consumption by optimizing both the operation of the combustion engine and the use of the battery capacity. For BEVs, predictions allow to determine the achievable driving range.

### 1.2. Literature

Such predictive information can then be exploited by the energy management system (EMS) of HEVs, various approaches to which have been studied in the literature throughout the last few decades. Based on the equivalent consumption minimization strategy (ECMS), a realization of Pontryagin's minimum principle (PMP) proposed by [4–6], the approaches of [7,8], for example, use predictive data to generate reference state of charge (SOC) trajectories that are then used in the on-line ECMS controller to prevent violating the admissible SOC window. The benefits of such approaches have been studied e.g. in [9], where it is shown that predictive grade profiles based on 3D terrain maps can improve the fuel economy on hilly driving missions by 1%–4%.

A more formal consideration of prediction updates and their horizon is followed by model predictive control (MPC). Here, an optimal control problem (OCP) is repeatedly solved by finding a control strategy on a receding prediction horizon of which only the first few inputs are applied until a new strategy is available. This control structure allows to handle highly nonlinear and interconnected systems with various input and output signals, many state variables, and various constraints. The underlying optimization problem may still be solved using PMP [10], but also other methods are popular, such as dynamic programming [11], or formulations as quadratic programs (QP) [12], convex programs [13], or nonlinear programs [14].

The EMS approaches mentioned above all consider the predictive data to be deterministic. However, predictive data is always subject to uncertainty and thus stochastic methods such as stochastic dynamic programming (SDP) and stochastic MPC (SMPC) have been proposed. Classic SDP typically is based on a homogeneous Markov chain that describes the probability of a sequence of future power requests based on the current measurement. The resulting infinite horizon problem can be solved offline using policy iteration [15], leading to a simple and efficient online controller that exploits the previously generated lookup tables [16]. Researchers have also studied position-dependent Markov chains [17], leading to a finite-horizon problem, which, according to the results obtained, is able to almost yield the global optimal fuel consumption. Despite these promising results, SDP suffers the so-called curse of dimensionality [18] and thus in general requires an offline optimization, which cannot take into account new data on the fly.

SMPC aims to close this gap by considering the uncertainty in both the system dynamics and the predictions via so-called chance constraints. Compared to robust MPC, where the constraints always have to be satisfied, SMPC allows to find an optimal control policy under uncertainty that is not overconservative but guarantees to fulfill the constraints with a certain predefined probability level. The resulting stochastic OCP is typically solved either by following an analytical propagation of the uncertainty or by using numerical approaches often referred to as scenario-based optimization [19]. The analytical approaches in general are limited to linear systems and simple probability distributions of the stochastic processes, such as the normal distribution. Only in specific cases, it has been shown that the tractability can be maintained throughout nonlinear systems. Scenario-based approaches, on the other hand, use Monte Carlo sampling techniques where the probability distributions can be of any form or even unknown. The only requirement is that a sufficient number of samples can be drawn from a random process, potentially also from a collection of historic data. The disadvantages of this method are that proofs of stability and recursive feasibility are currently still missing and that it entails a greater computational complexity. The former is considered a minor issue since the process is stochastic anyway and therefore, guarantees that such conditions are met often are not necessary. The latter, however, limits the capabilities of SMPC in real-time applications in terms of the system model complexity, the update frequency, the length of the prediction horizon, and the number of scenarios considered and thus the robustness level that can be achieved.

Many online applications proposed in the literature therefore consider short prediction horizons or horizons which are coarsely sampled. Regarding EMS of HEVs, for example, [20] use 11 sample points within a horizon of 120 s to obtain a velocity prediction and [21] use scenario trees with variable prediction lengths of 100 s at most to estimate the power request.

### 1.3. Research statement

To the best of the authors' knowledge, real-time EMS controllers based on long prediction horizons subject to uncertainty have not been addressed in the literature so far. The consideration of long horizons is, however, particularly relevant for vehicles with large battery capacities and is ideally realized through stochastic optimization, as pointed out in [22]. This requirement becomes even more apparent when the primary energy source is not always available, such as for trucks with partial overhead lines, trolley buses, or future scenarios where the operation of combustion engines may no longer be allowed in city centers. The problem on which we focus in this paper is therefore a methodology for efficiently integrating long prediction horizons subject to uncertainty into a stochastic optimization problem that can continuously improve itself with new experience.

### 1.4. Contribution

The main research contribution of this paper is a novel usage of PMP to formulate scenario programs that consider long prediction horizons subject to uncertainty. We show that a segmented power request trajectory can be represented by a sequence of a quadratic functions, each describing the energy supply required to obtain a certain change in SOC in the corresponding segment. Using these quadratic approximations, we formulate computationally efficient scenario programs that are capable of simultaneously considering hundreds of scenarios. Accordingly, they are applicable in online SMPC. The resulting scenario-based MPC (SCMPC) is demonstrated in a case study, which addresses the EMS of battery-assisted trolley buses that are equipped with batteries in order to bridge grid-free sections of bus routes.

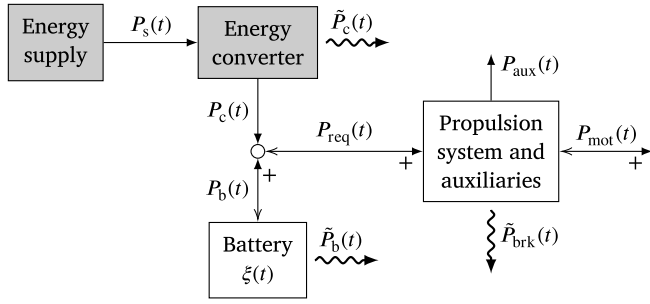


Fig. 1. Modeled energy flows in hybrid electric vehicles. Filled arrows indicate positive power flows, open arrows indicate negative power flows. Wavy arrows indicate losses. The boxes in gray represent a generic power supply chain and are to be replaced with a vehicle-dependent model.

### 1.5. Paper structure

The remainder of this paper is structured as follows: Section 2 presents the powertrain models used throughout the text and discusses the optimal control problem present in HEVs. In Section 3, we present the procedure by which a segment of a recorded power request signal can be approximated as a quadratic function. Section 4 validates this approximation by comparing the result obtained to an optimal reference in two separate studies, first on a battery-assisted trolley bus and second on a series HEV passenger car. The quadratic functions are then used in Section 5 to approximate the stochastic optimization problem as a scenario program. Section 6 exploits the resulting formulation within an MPC framework and demonstrates its applicability in a case study. Finally, Section 7 discusses the conclusions and proposes future work.

## 2. Optimal control problem in hybrid electric vehicles

### 2.1. Model of the powertrain

Fig. 1 shows the main components and power flows of a generic hybrid electric powertrain. The energy may be supplied by any sort of energy source such as fuel, hydrogen, or electricity. Accordingly, the energy converter can be realized with an internal combustion engine, a fuel cell, or an electric power converter. Supplied by the power  $P_s(t)$ , this unidirectional conversion provides the output power  $P_c(t)$  and causes the conversion losses  $\tilde{P}_c(t)$ . The energy storage device, illustrated here as an electrochemical battery, provides the output power  $P_b(t)$  by reducing the internal state of charge  $\xi(t)$  and incurring the conversion losses  $\tilde{P}_b(t)$ .

Assuming that the vehicle parameters are fixed, the mechanical power required to follow a certain driving mission can be calculated via the longitudinal vehicle dynamics [23] independently of and prior to the optimization, i.e.,

$$P_{\text{mot}}(t) = m v(t) \cdot (\dot{v}(t) + c_r g \cos \alpha(t) + g \sin \alpha(t)) + \frac{1}{2} \rho_{\text{air}} c_d A_f v(t)^3, \quad (1)$$

where  $v(t)$  is the vehicle speed and  $\alpha(t)$  is the road grade. The vehicle parameter  $m$  denotes the vehicle mass,  $c_r$  and  $c_d$  are the coefficients for the rolling friction and the aerodynamic drag, respectively, and  $A_f$  is the frontal area. The physical quantities  $\rho_{\text{air}} = 1.225 \text{ kg/m}^3$  and  $g = 9.81 \text{ m/s}^2$  denote the air density and the gravitational acceleration, respectively. If in addition, the traction power is provided exclusively by electric motors, which is the assumption made throughout this text, we can also directly calculate the power request  $P_{\text{req}}(t)$ . We assume an auxiliary power consumption  $P_{\text{aux}}(t)$  and a constant efficiency  $\eta$  for the electric motors, such that the electric power request is expressed as follows [23]:

$$P_{\text{req}}(t) = P_{\text{aux}}(t) + \tilde{P}_{\text{brk}}(t) + P_{\text{mot}}(t) \cdot \eta^{-\text{sign}(P_{\text{mot}}(t))}, \quad (2)$$

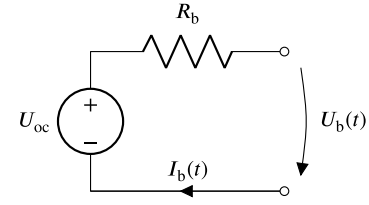


Fig. 2. Equivalent circuit model of the battery.

where  $\tilde{P}_{\text{brk}}(t)$  denotes the power dissipated in the mechanical brakes.

In order to simplify the notation of the remaining parts of the powertrain, we define the following two functions to denote the battery dynamics and the converter model, respectively,

$$\frac{d\xi(t)}{dt} = f_b(P_b(t)), \quad (3)$$

$$P_s(t) = f_c(P_c(t)). \quad (4)$$

Furthermore, we use two distinct vehicle models throughout this text, i.e., a series HEV and a battery-assisted trolley bus. While the battery model presented in Section 2.1.1 is independent of the vehicle type, the converter model is specific to the vehicle type. The two variants are introduced in Sections 2.1.2 and 2.1.3, respectively.

#### 2.1.1. Battery model

The battery is modeled assuming an equivalent circuit model as shown in Fig. 2, with both the battery internal resistance  $R_b$  and the open-circuit voltage  $U_{oc}$  being constant. This assumption typically holds well within the desired operating range of modern lithium-based batteries [24]. The power delivered by the battery is described by

$$P_b(t) = I_b(t) \cdot U_b(t), \quad (5)$$

where  $U_b(t)$  is the terminal voltage and  $I_b(t)$  is the battery current that discharges the battery for positive values. According to Kirchhoff's voltage law, we obtain

$$I_b(t) = \frac{1}{2 R_b} \left( U_{oc} - \sqrt{U_{oc}^2 - 4 R_b P_b(t)} \right), \quad (6)$$

which introduces the following constraint on the battery power:

$$P_b(t) \leq \frac{U_{oc}^2}{4 R_b}. \quad (7)$$

Using a Coulombic efficiency of 1, the dynamics of the SOC is given by its time-derivative,

$$\frac{d\xi(t)}{dt} = \frac{-I_b(t)}{Q_0}, \quad (8)$$

where  $Q_0$  is the charge capacity of the battery. Accordingly, the battery dynamics model (3) is given by

$$f_b(P_b(t)) = -\frac{1}{2 R_b Q_0} \left( U_{oc} - \sqrt{U_{oc}^2 - 4 R_b P_b(t)} \right). \quad (9)$$

#### 2.1.2. Converter model for a battery-assisted trolley bus

A battery-assisted trolley bus is a trolley bus equipped with a traction battery in order to bridge certain sections of the bus routes without overhead lines. Its powertrain is very similar to that of a plug-in HEV, with the overhead lines in place of the engine-generator unit (EGU). As shown in Fig. 3, the power supplied by the feed points of the electric grid is transmitted via the overhead lines to the trolley poles of the bus, where the unidirectional DC-DC converter is used to convert the current from the voltage level of the overhead lines to that of the battery. The electric circuit of the overhead lines is modeled as an ideal voltage source, representing the constant voltage  $U_g$  of the feed points, in series with a constant resistance  $R_g$ , which captures the transmission

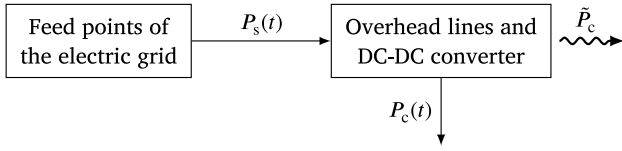


Fig. 3. Model of the power supply chain of the battery-assisted trolley bus, which completes the vehicle model by replacing the generic model blocks shown in Fig. 1.

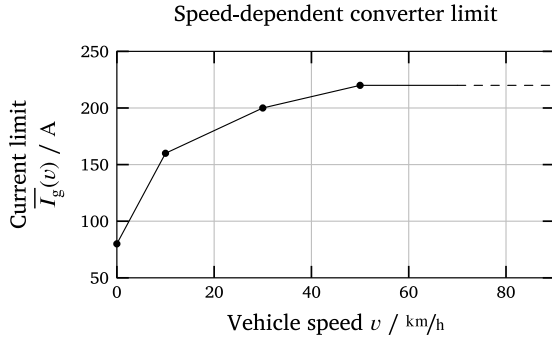


Fig. 4. The speed-dependent converter limit, which prevents an accelerated wear of the trolley shoes and the overhead lines.

losses. Hence, the model is similar to that of the battery shown in Fig. 2. The power supplied to the electric grid is

$$P_s(t) = U_g \cdot I_g(t), \quad (10)$$

where  $I_g(t)$  is the electric current flowing from the feed points to the trolley poles of the bus. The power that arrives at the trolley poles is given by

$$P_p(t) = (U_g - R_g \cdot I_g(t)) \cdot I_g(t). \quad (11)$$

The converter itself is modeled using a Willans approach [23], which describes the converter output power as an affine relation of the electric power at the trolley poles, i.e.,

$$P_c(t) = e P_p(t) - P_0, \quad (12)$$

where both the indicated conversion efficiency  $e$  and the idle losses  $P_0$  are constant model parameters. As a result, the combination of the overhead lines and the DC-DC converter is modeled as follows:

$$\begin{aligned} f_c(P_c(t)) &= U_g \cdot I_g(t) \\ &= \frac{U_g}{2R_g} \left( U_g - \sqrt{U_g^2 - 4R_g P_p(t)} \right) \\ &= \frac{U_g}{2R_g} \left( U_g - \sqrt{U_g^2 - 4R_g \frac{P_c(t) + P_0}{e}} \right), \end{aligned} \quad (13)$$

which limits the converter output power to

$$P_c(t) \leq \frac{e U_g^2}{4R_g} - P_0. \quad (14)$$

In addition, the current that can be drawn from the grid is limited in order to prevent excessive wear due to heat buildup between the trolley shoes and the overhead lines. This limit is speed-dependent, as shown in Fig. 4. It can be translated to an upper bound for the converter power via (11) and (12), such that

$$P_c(t) \leq \bar{P}_c(v(t)) = e \cdot (U_g - R_g \cdot \bar{I}_g(v(t))) \cdot \bar{I}_g(v(t)) - P_0. \quad (15)$$

### 2.1.3. Converter model for a series HEV

A classical series HEV is propelled by an electric motor only. The electric power is provided by the battery and an EGU, which is sometimes also referred to as an auxiliary power unit [23]. The energy may

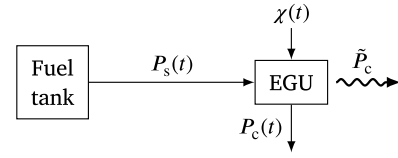


Fig. 5. Model of the power supply chain of the series HEV, which completes the vehicle model by replacing the generic model blocks shown in Fig. 1.

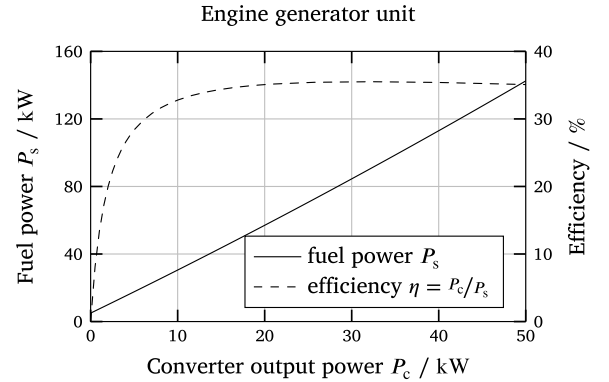


Fig. 6. Model of the engine generator unit (EGU).

be supplied by gasoline, Diesel, or natural gas, which is converted into electrical energy via the EGU, as shown in Fig. 5. In the context of this paper, we keep the exact specification open and discuss the chemical power of the fuel  $P_s(t)$  instead.

Since the engine is only mechanically connected to the generator, the rotational speed of both devices is independent of the vehicle speed. It therefore represents a degree of freedom which can be exploited by a lower-level controller in order to maximize the conversion efficiency. As a result, the required fuel power can directly be described as a function of the electrical output power, which can be approximated well via a quadratic function [25],

$$f_c(P_c(t)) = \chi(t) \cdot (\alpha_1 P_c(t)^2 + \alpha_2 P_c(t) + \alpha_3), \quad (16)$$

where the constraint  $P_c(t) \leq \chi(t) \cdot \bar{P}_c$  is required for consistency and the variable  $\chi(t)$  is introduced to describe the switching behavior, i.e.,

$$\chi(t) = \begin{cases} 1 & \text{if EGU is running,} \\ 0 & \text{otherwise.} \end{cases} \quad (17)$$

An illustration of the EGU model is shown in Fig. 6.

### 2.2. Problem formulation

We assume problem feasibility, i.e.,

$$P_{\text{req}}(t) \leq \widehat{P}_b + \widehat{P}_c \quad \forall t, \quad (18)$$

where

$$\widehat{P}_b = \min \left\{ \bar{P}_b, \frac{U_{\text{DC}}^2}{4R_b} \right\} \quad (19)$$

respects the constant battery discharge power limit  $\bar{P}_b$  and the physical limit (7) and

$$\widehat{P}_c = \begin{cases} \chi(t) \cdot \bar{P}_c & \text{for a series HEV,} \\ \min \left\{ \bar{P}_c(v(t)), \frac{e U_g^2}{4R_g} - P_0 \right\} & \text{for a trolley bus,} \end{cases} \quad (20)$$

which is either defined by the maximum EGU output power in the case of a series HEV, or by (14) and (15) in the case of a battery-assisted

trolley bus. In addition, we can assume that

$$P_{\text{req}}(t) \geq \underline{P}_b \quad \forall t, \quad (21)$$

where  $\underline{P}_b$  is the constant battery charge power limit. This limit does not restrict our choice of the driving mission since excess braking power can always be dissipated in the mechanical brakes via  $\hat{P}_{\text{brk}}(t)$ .

The goal of the OCP for HEVs is to satisfy the power request  $P_{\text{req}}(t)$  for all  $t \in [t_0, t_f]$  by the converter and the battery such that the total energy supply  $E_s = \int_0^{t_f} P_s(t) dt$  is minimized and all operating limits of all devices are always respected. Furthermore, for conventional HEVs, typically charge sustenance is required, meaning that the final and initial SOC of the battery should be equal. For plug-in HEVs, on the other hand, this challenge is often omitted due to the lower price and emission levels of electricity, leading to a charge-depleting strategy.

The deterministic OCP can thus be written as in the following. According to (18) and (21), the power balance  $P_{\text{req}}(t) = P_b(t) + P_c(t)$  is always satisfied with equality such that the OCP can be formulated with only one degree of freedom, namely  $P_b(t)$ .

$$\begin{aligned} \min_{P_b(t)} \quad & \int_{t_0}^{t_f} P_s(t) dt \\ \text{s.t.} \quad & P_{\text{req}}(t) = P_b(t) + P_c(t), \\ & \frac{d}{dt} \xi(t) = f_b(P_b(t)), \\ & P_s(t) = f_c(P_c(t)), \\ & \xi(t) \in [\underline{\xi}, \bar{\xi}], \\ & P_b(t) \in [\underline{P}_b, \widehat{P}_b], \\ & P_c(t) \in [0, \widehat{P}_c], \\ & \xi(t_0) = \xi_{\text{init}}, \\ & \xi(t_f) = \xi_{\text{final}}, \end{aligned} \quad (22)$$

where the lower and upper bounds of the SOC are denoted by  $\underline{\xi}$  and  $\bar{\xi}$ , respectively. The initial and final SOC are denoted by  $\xi_{\text{init}}$  and  $\xi_{\text{final}}$ , respectively.

### 2.3. Stochastic OCP

In this section, we introduce the stochastic OCP using chance constraints on the system state, i.e., the SOC. A numerical approximation of (22) formulated as stochastic OCP follows, where the forward Euler method with a sample time of typically  $T_s = 1$  s is used for long-horizon applications:

$$\begin{aligned} \min_{\substack{P_{b,k} \in \mathbb{U}_k \\ \forall k \in \{1, \dots, K-1\}}} \quad & \sum_{k=1}^{K-1} \mathbb{E} \left[ f_c(P_{\text{req},k} - P_{b,k}) \cdot T_s \right] \\ \text{s.t.} \quad & \xi_{k+1} = \xi_k + f_b(P_{b,k}) \cdot T_s, \quad \forall k = 1, \dots, K-1, \\ & \Pr \left[ \xi_k \notin \mathbb{X} \right] \leq \epsilon, \quad \forall k = 1, \dots, K-1, \\ & \xi_1 = \xi_{\text{init}}, \\ & \xi_K = \xi_{\text{final}}. \end{aligned} \quad (23)$$

Each stage cost is taken in expectation  $\mathbb{E}[\cdot]$  since  $P_{\text{req}} \in \mathbb{R}^{K-1}$  is now considered to be a random variable. Hence, also  $P_b \in \mathbb{R}^{K-1}$  and  $\xi_2, \dots, \xi_{K-1}$  are random variables. The state constraints are formulated as chance constraints with the violation parameter  $\epsilon \in (0, 1)$ . The state constraint set  $\mathbb{X}$  and the set of feasible inputs  $\mathbb{U}_k$  are defined by

$$\mathbb{X} = \left[ \underline{\xi}, \bar{\xi} \right], \quad (24)$$

$$\mathbb{U}_k = \left[ \max \left\{ P_{\text{req},k} - \widehat{P}_c, \underline{P}_b \right\}, \min \left\{ P_{\text{req},k}, \widehat{P}_b \right\} \right], \quad (25)$$

respectively, where the latter can be formulated on account of (18) and (21) and thus ensures that all component constraints are satisfied.

Stochastic OCPs such as the one presented in (23) are generally difficult to solve. Even if  $\mathbb{X}$  is a convex set, the feasible set described by the chance constraints in general is not [26]. Therefore, we follow the scenario approach [27] to approximate (23), which has the additional benefit of being purely data-driven and independent of the underlying mechanisms by which uncertainty is generated. Replacing the chance constraints with regular constraints and using an appropriate objective function, the goal of the scenario-based OCP is to find an appropriate control strategy for a given number of scenarios such that all constraints are satisfied for all of those scenarios. The required number of scenarios to achieve a reasonably small risk is usually in the range of a few hundreds, which strongly limits the complexity of the stochastic OCP (23) and in particular the number of decision variables  $K$ . To mitigate this limitation, we exploit the theoretical results of Pontryagin's minimum principle. The corresponding formulation significantly reduces the number of decision variables, while still maintaining a final control policy that is easy to evaluate and optimal for each point in time.

### 3. Approximation using Pontryagin's minimum principle

The theory of PMP [28] states that the solution to an optimal control problem is fully characterized by a constant value of the Lagrange multiplier  $\lambda$ , also referred to as the costate variable, as long as the state trajectory is within the admissible bounds and neither the objective function nor the state equation depends on the state itself. This property renders EMS an ideal application, as studied by many researchers, see e.g., [6,23,24].

In the following sections, a brief description of the standard realization of PMP for the energy management of HEVs is provided for completeness. We then present an alternative solution method based on a fragmentation of the driving mission, the result of which is then used to formulate the scenario program approximating (23).

#### 3.1. Pontryagin's minimum principle

A thorough description and derivation of PMP can be found in the book on optimal control of HEVs [29]. The theory provides a set of necessary conditions that the optimal solution must satisfy, which turns out to be also sufficient if the Hamiltonian function is strictly convex in the control variable [6]. The solution to the OCP can then be obtained by solving the so-called Hamiltonian system, which is a two-point boundary value problem (TPBVP).

With regard to the energy management of HEVs, the corresponding Hamiltonian function is defined as

$$\begin{aligned} H(P_{\text{req}}(t), P_b(t); \lambda) &= P_s(t) + \lambda \cdot f_b(P_b(t)) \\ &= f_c(P_{\text{req}}(t) - P_b(t)) + \lambda \cdot f_b(P_b(t)). \end{aligned} \quad (26)$$

Both the objective function and the state update function (9) are independent of the SOC, the latter due to the assumption of  $U_{\text{oc}}$  being constant. As a result, the costate variable  $\lambda(t)$  is a piecewise constant function in general. If the state constraints are not violated by the optimal solution,  $\lambda$  becomes a constant. Accordingly, the TPBVP can be solved using a single shooting method in conjunction with a root finding algorithm, for which the bisection method has shown to be most suitable [30]. However, in the presence of active state constraints, additional jump conditions need to be taken into account. A solution to this problem is presented in [31], where the horizon of the problem is recursively subdivided at instances where the most severe constraint violations would occur if a constant solution of the TPBVP was used. The resulting costate trajectory is shown to be the globally optimal solution if the OCP has certain convexity properties. Moreover, if the Hamiltonian function is not convex, e.g. due to on/off switching of an internal combustion engine, the optimal control policy often is not unique. In fact, without taking the corresponding singularity into account, a desired target SOC is usually not exactly reachable [32,33].

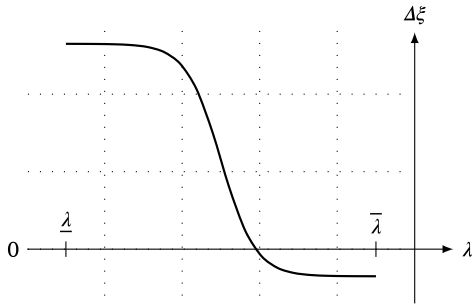


Fig. 7. Typical shape of the change in SOC  $\Delta\xi^{(i)} = f_{\xi}^{(i)}(\lambda)$  on a given segment  $i$  as a function of  $\lambda \in [\underline{\lambda}, \bar{\lambda}]$ .

In the interest of a better readability, we continue with the assumption of no state constraint violations and no singular control problem, while keeping in mind that methods exist for addressing the general case. The solution of the OCP is then obtained numerically by finding the optimal value of  $\lambda^*$  such that

$$\xi_{\text{init}} + \int_{t_0}^{t_f} f_b(P_b^*(t)) dt = \xi_{\text{final}}, \quad (27)$$

where  $P_b^*(t) = P_b(t; \lambda^*)$  and

$$P_b(t; \lambda) = \arg \min_{P_b(t)} \left( H(P_{\text{req}}(t), P_b(t); \lambda) \right). \quad (28)$$

On the account of the definitions  $f_b(P_b(t))$  and  $f_c(P_c(t))$ , it follows that  $\lambda \leq 0$ . Therefore, in ECMS, typically a variable  $s \geq 0$  proportional to  $-\lambda/(U_{\text{oc}} \cdot Q_0)$  is defined as the “equivalence factor” [24], such that the intrinsic trade-off between the power being supplied and the power being drawn from the battery appears more intuitively. In the course of this paper, however, we keep the costate variable  $\lambda \in \mathbb{R}_{\leq 0}$  such that its values are given in the physical unit of energy. For the numerical integration of (27), the forward Euler method with  $T_s = 1$  s is used as in (23). The solution of (28) can be found either numerically, using gradient-based methods or grid search, or analytically for certain problems, as shown in Sections 4 and 6 below.

### 3.2. Direct multiple shooting

Instead of the single shooting method described above, the solution to the TPBVP can also be obtained by dividing the horizon of the problem into several segments and applying direct multiple shooting [34]. In each segment  $i \in \{1, \dots, M\}$  defined by the start time  $t_0^{(i)}$  and the end time  $t_f^{(i)}$ , we calculate the change in SOC as a function of  $\lambda$  using

$$\Delta\xi^{(i)} = f_{\xi}^{(i)}(\lambda) = \int_{t_0^{(i)}}^{t_f^{(i)}} f_b(P_b(t; \lambda)) dt, \quad (29)$$

where  $P_b(t; \lambda)$  is parameterized by  $\lambda \in [\underline{\lambda}, \bar{\lambda}]$  as in (28). A typical shape of this function is shown in Fig. 7. The exact form of  $f_{\xi}^{(i)}(\lambda)$  depends on the power request trajectory  $P_{\text{req}}(t)$  within  $t_0^{(i)} \leq t \leq t_f^{(i)}$ . Fig. 7 shows that changes in SOC saturate on both ends of the spectrum of  $\lambda$ , which is due to the specific realization of the power request trajectory  $P_{\text{req}}(t)$  and the physical limitations of the system. Reasonable values for a lower bound  $\underline{\lambda}$  and an upper bound  $\bar{\lambda}$  can thus be found experimentally. If  $\lambda$  is near  $\underline{\lambda}$ , the battery is charged as much as possible within this segment. If  $\lambda$  is near  $\bar{\lambda}$ , a battery-depleting strategy results. While in both of these regions, changes in  $\lambda$  have only a limited effect on the change in SOC, the strategy is very sensitive to changes in the middle range of  $\lambda$ .

Similarly to (29), the energy supply of each segment is obtained as a function of  $\lambda$  as follows:

$$E_s^{(i)} = f_{E_s}^{(i)}(\lambda) = \int_{t_0^{(i)}}^{t_f^{(i)}} f_c(P_{\text{req}}(t) - P_b(t; \lambda)) dt, \quad (30)$$

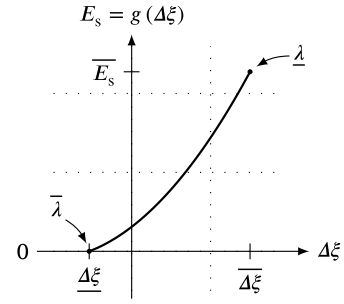


Fig. 8. Typical shape of the energy supply  $E_s^{(i)} = g^{(i)}(\Delta\xi^{(i)})$  on a given segment  $i$  as a function of the change in SOC  $\Delta\xi^{(i)}$ , parameterized by  $\lambda \in [\underline{\lambda}, \bar{\lambda}]$ .

Combining (29) and (30), we can describe a mapping for each segment  $i$ ,

$$\lambda \mapsto \left( \Delta\xi^{(i)}, E_s^{(i)} \right), \quad (31)$$

for  $\lambda \in [\underline{\lambda}, \bar{\lambda}]$ . Using the following definition for the domain on segment  $i$ ,

$$\mathbb{W}^{(i)} = \left[ \underline{\Delta\xi}^{(i)}, \overline{\Delta\xi}^{(i)} \right], \quad (32)$$

we can define the mapping  $g^{(i)}$ , i.e.,

$$g^{(i)} : \mathbb{W}^{(i)} \rightarrow \left[ 0, \overline{E_s}^{(i)} \right], \quad (33)$$

$$\Delta\xi^{(i)} \mapsto E_s^{(i)},$$

a typical shape of which is shown in Fig. 8. Having such a mapping for each of the segments of the horizon, we can approximate the deterministic OCP defined in (22) as follows:

$$\begin{aligned} \min_{\Delta\xi^{(i)} \in \mathbb{W}^{(i)} \forall i \in \{1, \dots, M\}} & \sum_{i=1}^M g^{(i)}(\Delta\xi^{(i)}) \\ \text{s.t.} & \xi_{\text{init}} + \sum_{i=1}^m \Delta\xi^{(i)} \in \mathbb{X}, \quad \forall m = 1, \dots, M, \\ & \xi_{\text{init}} + \sum_{i=1}^M \Delta\xi^{(i)} = \xi_{\text{final}}, \end{aligned} \quad (34)$$

where the decision variables are the change in SOC in each segment and the objective function is the sum of the corresponding energy supply values that are required to achieve the changes in SOC. The two constraints ensure that the SOC remains within the admissible window and that the solution is charge sustaining, respectively.

The mappings (33) can be evaluated numerically by interpolating the values of (31) calculated on a sufficiently sampled numerical range of  $\lambda$ . Alternatively, as motivated by Fig. 8, the mappings can also be approximated quite well with a quadratic relation, i.e.,

$$g^{(i)}(\Delta\xi^{(i)}) \approx \hat{g}^{(i)}(\Delta\xi^{(i)}) = p_3^{(i)} + p_2^{(i)} \cdot \Delta\xi^{(i)} + p_1^{(i)} \cdot \left( \Delta\xi^{(i)} \right)^2, \quad (35)$$

which converts (34) into a QP if  $p_1^{(i)} \geq 0 \forall i$ . The parameters  $p_1^{(i)}$ ,  $p_2^{(i)}$ , and  $p_3^{(i)}$  can be obtained independently for each segment prior to the optimization, e.g. by using the method of least squares. This “encoding” allows to represent the power request  $P_{\text{req}}(t)$  by a sequence of  $M$  tuples, each of which represents the corresponding segment  $i$  with only three parameters  $(p_1^{(i)}, p_2^{(i)}, p_3^{(i)})$ . Section 5 is to show that this encoding allows the formulation of an SMPC strategy that is able to consider long prediction horizons with a reduced number of decision variables and constraints.

## 4. Validation of the OCP approximation

At this point it is useful to present a validation of the claims made above, particularly the statement that the combination of (34) and (35)

**Table 1**  
Parameters for the trolley bus case study.

$m$	Vehicle mass	23 000 kg
$A_f$	Frontal area	8.67 m <sup>2</sup>
$c_d$	Aerodynamic drag coefficient	0.9
$c_r$	Rolling friction coefficient	0.009
$\eta$	Traction motor efficiency	0.9
$P_{aux}$	Auxiliary power	10 kW
$R_b$	Battery internal resistance	0.1 $\Omega$
$U_{oc}$	Battery open circuit voltage	750 V
$Q_0$	Battery charge capacity	80 Ah
$\bar{P}_b$	Maximum battery discharge power	350 kW
$\underline{P}_b$	Maximum battery charge power	-350 kW
$\bar{\xi}$	Upper SOC bound	90%
$\underline{\xi}$	Lower SOC bound	50%
$e$	Indicated conversion efficiency	0.95
$P_0$	DC-DC converter idle loss	200 W
$U_g$	Grid voltage (at the feed point)	680 V
$R_g$	Grid resistance	0.4 $\Omega$

is an appropriate approximation of the original problem (22). To do so, we adopt (1) and (2) to calculate the power request to follow the velocity profiles of the worldwide harmonized light-duty vehicles test cycle (WLTC). The elevation profile is assumed to be flat. As for the vehicle type, we study a battery-assisted trolley bus modeled as described in Section 2.1.2 and a series HEV passenger car based on the models presented in Section 2.1.3. In both cases, the power request trajectory is split every 2 km into  $M$  distinct segments, with the remainder added to the last one. The chosen length allows for a clear representation of the results, but is somewhat arbitrary, as Section 4.3 is to elaborate in more detail. For each segment  $i \in \{1, \dots, M\}$ , we choose several values of  $\lambda \in [\underline{\lambda}, \bar{\lambda}] \subseteq \mathbb{R}_{\leq 0}$  and calculate  $\Delta \xi^{(i)}$  and  $E_s^{(i)}$  according to (29) and (30), respectively. The resulting data points are then approximated as a quadratic relation (35), for which constrained linear least squares is used. Moreover, the data values for  $\Delta \xi^{(i)}$  are first multiplied by  $Q_0 \cdot U_{oc}$  such that both the domain and the co-domain are stated in physical units of energy. After solving (34) with the quadratic approximation  $\hat{g}^{(i)}$  instead of  $g^{(i)}$ , we invert the relation (29) illustrated in Fig. 7 to obtain the costate values that correspond to the optimal values of  $\Delta \xi^{(i)}$ . Based on the resulting piecewise constant function of  $\lambda(t)$ , the trajectories of the SOC and the energy supply are calculated via (29) and (30), respectively.

#### 4.1. Battery-assisted trolley bus

As a trolley bus is a heavy vehicle for inner-city driving, we make use of the Class 2 test cycle that consists of the three parts for low, medium, and high speed. The vehicle models are described in Sections 2.1.1 and 2.1.2. The parameters are listed in Table 1. The initial and final SOC are set to  $\xi_{init} = \xi_{final} = 70\%$ . Using (9) and (13), we can formulate the Hamiltonian function (26), the minimum of which can be found analytically via the roots of its derivative w.r.t.  $P_b(t)$ , which yields

$$P_b(t; \lambda) = \frac{4 \lambda^2 e R_g (P_{req}(t) + P_0) + U_g^2 (Q_0^2 U_{oc}^2 - \lambda^2 e^2)}{4 (\lambda^2 e R_g + U_g^2 Q_0^2 R_b)}. \quad (36)$$

A detailed derivation can be found in Appendix A. Since the Hamiltonian function is convex in  $P_b(t)$ , (36) provides the unique optimal solution if

$$P_b(t; \lambda) \in \left[ \max \left\{ P_{req}(t) - \widehat{P}_c, \underline{P}_b \right\}, \min \left\{ P_{req}(t), \widehat{P}_b \right\} \right], \quad (37)$$

analogously to (25). Otherwise, the upper and lower boundary values of the domain of (37) have to be considered, where the one leading to a smaller value of the Hamiltonian function represents the desired battery power.

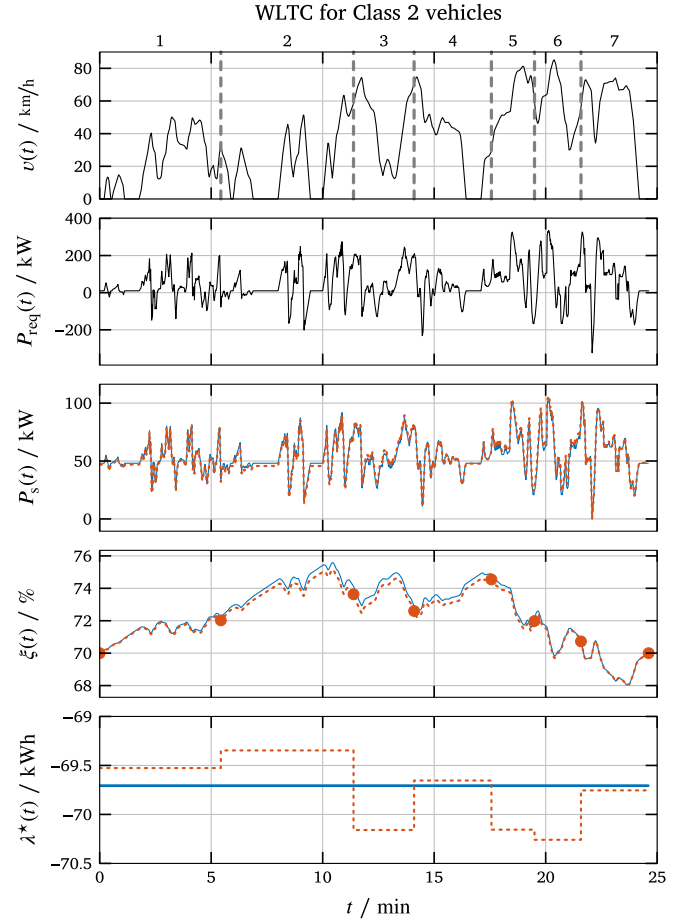


**Fig. 9.** Time-resolved results of simulating the trolley bus on the WLTC. The numbers and the dashed lines in the top graph indicate the 7 segments of this driving mission. For comparison, the optimal results of  $P_s(t)$ ,  $\xi(t)$ , and  $\lambda^*(t)$  using the single-shooting PMP (27) are shown in blue, while the QP approximation (34)–(35) is superimposed with dotted lines in red. The markers in the graph second to the bottom illustrate the SOC trajectory as optimized by (34).

The time-resolved results are shown in Fig. 9. Clearly, the difference in  $P_s(t)$  between the optimal solution and the quadratic approximation is very small. In fact, the energy supply in total is 22.27 kWh in both cases, which corresponds to 1.52 kWh/km. The difference between the two approaches becomes evident in  $\xi(t)$  and  $\lambda^*(t)$  where, however, the value range shown of the latter is very small. Both the quadratic approximations and the SOC difference as a function of  $\lambda \in [-100 \text{ kWh}, -50 \text{ kWh}]$  are illustrated in Fig. 10.

#### 4.2. Series HEV passenger car

In contrast to the trolley bus studied, a series HEV includes a binary control action for the engine on/off switch. As a result, the SOC differences (29) as a function of the costate typically are not well distributed, and the relations may even be discontinuous [33]. Therefore, unlike in Section 4.1, we now approach the mapping (33) from the other direction and solve a TPBVB for each of the desired target SOC differences using the strategy proposed in [33]. The results are shown in Fig. 11. We uniformly distribute 21 target SOC differences within a range of  $\pm 25\%$ . For the bisection method, we specify a search interval of  $\lambda \in [-3.5 \text{ kWh}, -2 \text{ kWh}]$ . The minimization of the Hamiltonian (26) is carried out for the two distinct cases (17) similarly to [25]. However, in contrast to the approximated quadratic loss model presented there, we use an algebraic solution of (28), the derivation of which is given in Appendix B.

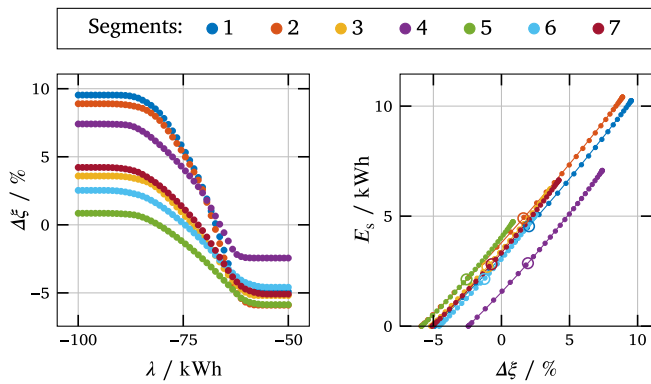


Fig. 10. SOC difference as a function of the costate and energy supply as a function of the SOC difference, both for the battery-assisted trolley bus. The dots of both graphs represent the calculated data values. The curves and the circles of the right graph represent the quadratic approximations and the solution of the quadratic program, respectively.

Table 2

Parameters for the series HEV case study.

$m$	Vehicle mass	1800 kg
$A_f$	Frontal area	2.2 m <sup>2</sup>
$c_d$	Aerodynamic drag coefficient	0.3
$c_r$	Rolling friction coefficient	0.01
$\eta$	Traction motor efficiency	0.9
$P_{aux}$	Auxiliary power	1.6 kW
$R_b$	Battery internal resistance	0.15 $\Omega$
$U_{oc}$	Battery open circuit voltage	400 V
$Q_0$	Battery charge capacity	2.5 Ah
$\bar{P}_b$	Battery discharge power limit	15 kW
$\bar{P}_c$	Battery charge power limit	-15 kW
$\xi_{\bar{c}}$	Upper SOC bound	90%
$\xi_{\bar{c}}$	Lower SOC bound	30%
$\bar{P}_c$	Maximum EGU output power	50 kW
$\alpha_1$	EGU polynom parameter	0.005 1/kw
$\alpha_2$	EGU polynom parameter	2.5
$\alpha_3$	EGU polynom parameter	5 kW

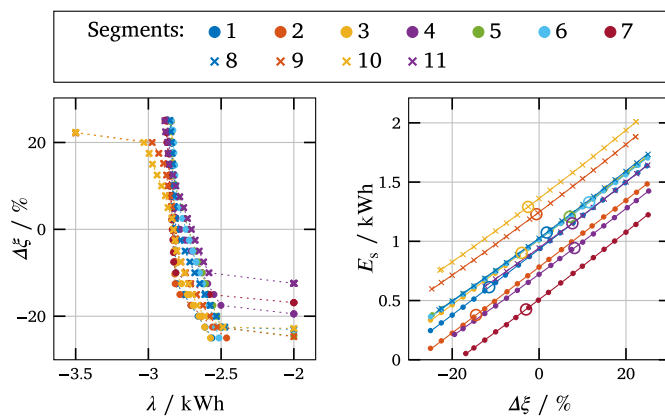


Fig. 11. SOC difference as a function of the costate and energy supply as a function of the SOC difference, both for the series HEV passenger car. The dots of both graphs represent the calculated data values. The curves and the circles of the right graph represent the quadratic approximations and the solution of the quadratic program, respectively.

In order to demonstrate the general applicability of the proposed method, we are using a medium-size passenger car with the parameters listed in Table 2, driven on the Class 3 test cycle. The initial and final SOC are set to  $\xi_{init} = \xi_{final} = 60\%$ . The driving mission and the chosen segments are shown in Fig. 12, along with the results of the

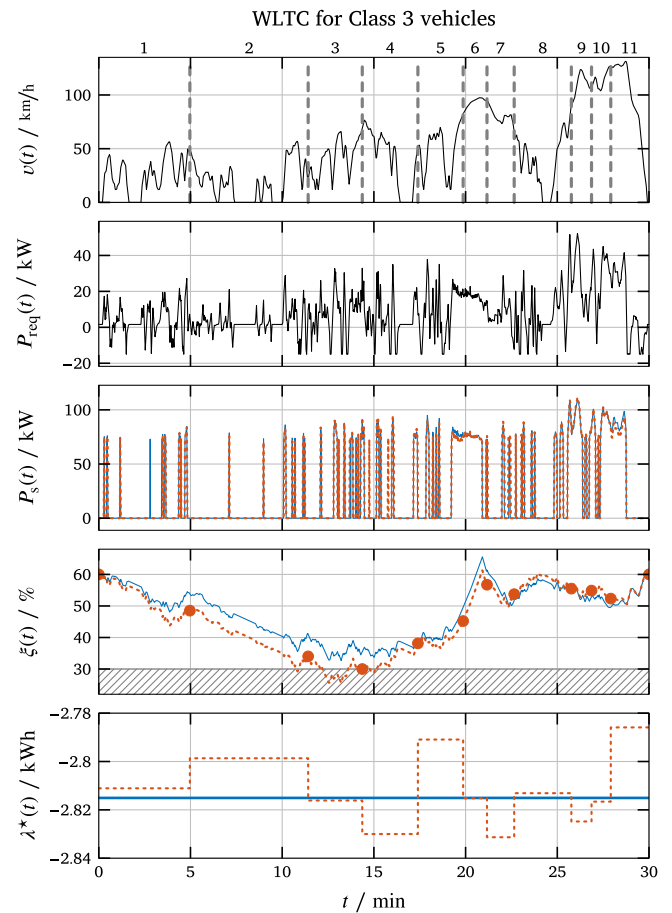


Fig. 12. Time-resolved results of simulating the series HEV passenger car on the WLTC. The numbers and the dashed lines in the top graph indicate the 11 segments of this driving mission. For comparison, the optimal results of  $P_s(t)$ ,  $\xi(t)$ , and  $\lambda^*(t)$  using the single-shooting PMP (27) are shown in blue, while the QP approximation (34)–(35) is superimposed with dotted lines in red. The markers in the graph second to the bottom illustrate the SOC trajectory as optimized by (34).

optimal single-shooting PMP (27) and the QP approximation (34)–(35). The corresponding energy supply is 10.67 kWh in both cases, which corresponds to a gasoline consumption of 5.18 l/100 km, using a lower heating value of 42.5 MJ/kg and a density of 0.75 kg/l. However, the SOC trajectories resulting from the optimal single-shooting PMP and the QP approximation are no longer as similar to each other as the ones shown in Fig. 9. The main reason for this discrepancy is found in the on/off behavior of the EGU, which has a decisive influence, especially at low loads. As a consequence, the relations between the costate and both the SOC difference (29) and the energy supply (30) are less smooth, which lead to a poorer approximation of  $g$ . In the specific example studied here, the optimization exploits this inaccuracy and depletes the battery faster in the first two segments, which is compensated for mainly in the fourth segment. The overall performance, however, is barely affected, as can be seen in the final consumption.

The only problematic aspect of using the proposed approximation is the loss of control over the SOC trajectories within the segments, as the violation of the lower SOC boundary within the third segment clearly shows.

#### 4.3. Remark on the lengths of the segments

Our experience with various simulations has shown that, in principle, the segment lengths can be chosen arbitrarily and have no relevant impact on the validity of the proposed approximation. Therefore, longer

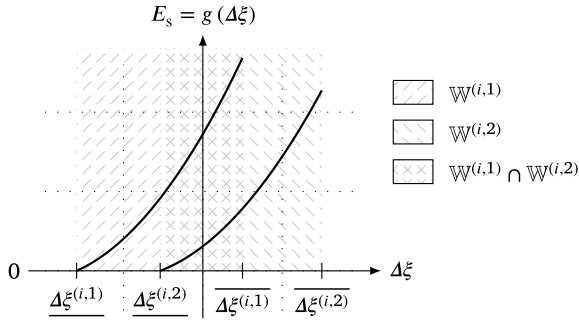


Fig. 13. Domain for the decision variable  $\Delta\xi^{(i)}$  of a specific segment  $i$ , assuming only two scenarios  $j \in \{1, 2\}$  for visual clarity. The domains  $\mathbb{W}^{(i,1)}$  and  $\mathbb{W}^{(i,2)}$  are as defined in (32). The domain for the decision variable  $\Delta\xi^{(i)}$  is given by the intersection  $\mathbb{W}^{(i,1)} \cap \mathbb{W}^{(i,2)}$ .

segments allow to increase the compression of the data, which leads to a smaller number of decision variables. However, since the optimization (34) can only constrain the SOC values at the edges of the segments, the trajectories within the segments are not constrained, which may lead to violations of the SOC bounds, as can be seen in Fig. 12. Accordingly, shorter segments increase the robustness of the approximation with respect to those bounds. In summary, the choice of the segment lengths allows a trade-off between the number of decision variables and the robustness of the approximation with respect to the admissible SOC window.

## 5. Scenario-based model predictive control

### 5.1. Scenario program with classic structure

In this section, we present the scenario program that approximates the stochastic OCP (23). Using the segment-based compression (33), the stochastic OCP (23) is approximated by the following scenario program, where the superscript  $(i, j)$  refers to the  $i$ th segment of the  $j$ th scenario,

$$\begin{aligned}
 \min_{\Delta\xi^{(i)}} \quad & \frac{1}{N} \sum_{j=1}^N \sum_{i=1}^M \hat{g}^{(i,j)}(\Delta\xi^{(i)}) \\
 \text{s.t.} \quad & \Delta\xi^{(i)} \in \bigcap_{j=1}^N \mathbb{W}^{(i,j)}, \quad \forall i = 1, \dots, M, \\
 & \xi_{\text{init}} + \sum_{i=1}^m \Delta\xi^{(i)} \in \mathbb{X}, \quad \forall m = 1, \dots, M, \\
 & \xi_{\text{init}} + \sum_{i=1}^M \Delta\xi^{(i)} = \xi_{\text{final}}.
 \end{aligned} \tag{38}$$

As in the classical scenario approach [27], each segment  $i$  corresponds to one control input  $\Delta\xi^{(i)}$ , which holds for all scenarios  $j \in \{1, \dots, N\}$ . Each of the  $N$  scenarios is thereby described by  $M$  mappings  $\hat{g}^{(i,j)}(\Delta\xi^{(i)})$ . The resulting energy supplies are aggregated using an average cost formulation. The  $M$  domain intersections ensure that each decision variable  $\Delta\xi^{(i)}$  remains feasible for all scenarios, an illustrative example of which is shown in Fig. 13.

However, these constraints can be very restricting and even lead to an infeasible problem if the individual domains of a certain segment do not overlap. Realizing, though, that due to the maximum charging capabilities, only the upper bounds of the intersections are actually restrictive, we can remove the lower bounds. As it is always possible to dissipate electric power, we only have to ensure that the corresponding energy supply is zero below those bounds, which is implemented using pointwise maxima [35]. In addition, to ensure feasibility for almost any scenario, the final state constraint is replaced by a soft constraint,

which is penalized via the hyperparameter  $\kappa$ . Finally, we drop the normalization in the objective function. Hence, (38) becomes

$$\begin{aligned}
 \min_{\Delta\xi^{(i)}} \quad & \sum_{j=1}^N \left[ \sum_{i=1}^M \max \left\{ 0, \hat{g}^{(i,j)}(\Delta\xi^{(i)}) \right\} \right] + \kappa \left( \xi_{\text{init}} + \sum_{i=1}^M \Delta\xi^{(i)} - \xi_{\text{final}} \right)^2 \\
 \text{s.t.} \quad & \Delta\xi^{(i)} \leq \min_j \left\{ \overline{\Delta\xi^{(i,j)}} \right\}, \quad \forall i = 1, \dots, M, \\
 & \xi_{\text{init}} + \sum_{i=1}^m \Delta\xi^{(i)} \in \mathbb{X}, \quad \forall m = 1, \dots, M,
 \end{aligned} \tag{39}$$

where  $\kappa$  needs to be large enough such that the final SOC constraint is satisfied whenever possible.

### 5.2. Discussion on generalization

Intuitively, the more scenarios are used, the harder it becomes to satisfy all constraints of (39) and the greater the objective value becomes, and vice versa. However, in order to keep the probability of violating the SOC constraints below a certain level  $\epsilon$ , a sufficiently large number of scenarios has to be taken into account. This mathematical relationship is referred to as the generalization theory.

In the classic scenario approach [27], it translates to the following condition, which holds for convex problems and identically and independently distributed (i.i.d.) scenarios. If

$$N \geq \frac{2}{\epsilon} \left( \ln \frac{1}{\beta} + M \ln 2 \right), \tag{40}$$

then, with probability of at least  $1 - \beta$ , the probability of violating the SOC constraints is at most  $\epsilon$ . As the confidence parameter  $\beta \in (0, 1)$  accounts for the possibility that the sampled scenarios cover only a small amount of the probability mass, it typically is assigned a rather small number. The lower bound (40), however, is tight only for fully supported problems, where the number of optimization variables is equal to the number of support constraints. A support constraint is defined as a constraint, the removal of which causes a change in the solution of the program. For convex problems, the support constraints are a subset of the active constraints.

Hence, for most practical applications, (40) is too conservative, which has prompted further research in various directions aiming at finding tighter bounds for the required number of scenarios [19,26,36–38]. Another direction is proposed by [39,40], where the number of support constraints is evaluated after solving the problem. Under the assumption of existence and uniqueness and non-degeneracy of the problem, upper and lower bounds for the risk, i.e., the probability of constraint violation, are derived in [40]. These confidence regions are shown in Fig. 14 for various numbers of scenarios and values of the confidence parameter  $\beta$ . With high confidence  $1 - \beta$ , the risk for the solution to violate a new, out-of-sample, state constraint  $\xi \in \mathbb{X}$  is within the corresponding interval  $[\underline{\epsilon}(n_s), \bar{\epsilon}(n_s)]$ , where  $n_s$  is the number of support constraints observed. According to [41], the assumption of non-degeneracy can even be dropped and the number of support constraints can be replaced by the number of active constraints.

As a conclusion, if typically only a few constraints of the problem are active, the a posteriori evaluation of the violation probability offers the advantage that much fewer scenarios have to be considered for the same violation level. Accordingly, it allows the treatment of problems with a much larger number of decision variables. However, since the violation level can only be estimated after the problem has been solved, no guarantees for a generalization can be given beforehand. Thus, if required by a particular application, (40) or appropriate improvements from the aforementioned references must be consulted.

With regard to the EMS of HEVs, this discussion boils down to the length and the discretization of the prediction horizon. If, for example, the segments have a length of 500 m and the prediction horizon is 5 km, according to (40), the violation probability is guaranteed to be below 5% with a probability of 99.9% if  $N \geq 550$ , which is a feasible

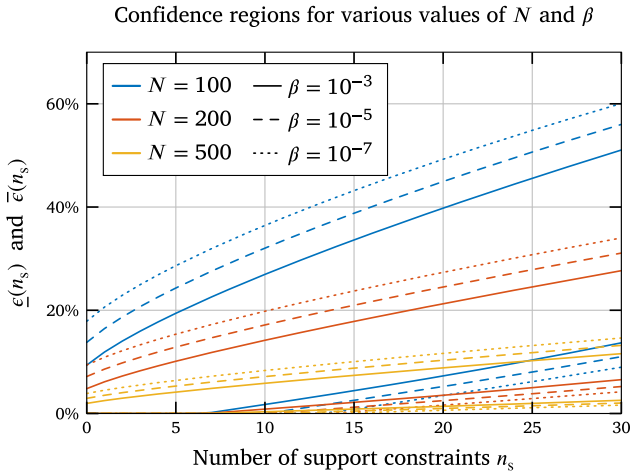


Fig. 14. Theoretical bounds on the risk, i.e., the probability of violating new, out-of-sample, constraints according to [40]: The risk for the solution to violate the random constraints is within the interval  $[\underline{\epsilon}(n_s), \bar{\epsilon}(n_s)]$  with confidence  $1 - \beta$ .

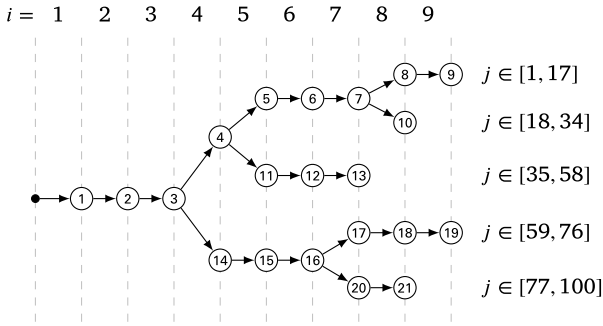


Fig. 15. Illustration of a scenario tree based on  $N = 100$  scenarios. Each vertex represents one decision variable  $\Delta\xi^\ell$ , indexed by  $\ell$ . The variable  $i$  denotes the segment or level. The branches of the tree can be of different lengths and can represent different numbers of scenarios  $j$ .

number in practice. On the other hand, if the segments should be shorter and the horizon should be longer, the classic scenario approach quickly becomes impractical. In addition, in case the scenarios are substantially different because they branch out in different directions at road junctions, for example, a single sequence of decision variables might not be able to meet all constraints of the problem anymore. Hence, a different structure than the classic formulation of the scenario program is required, which introduces even more decision variables.

### 5.3. Scenario program with tree structure

One such alternative formulation to the classic scenario approach is proposed by [21]. The authors expand a scenario tree in the most likely direction, where a separate decision variable is associated to each vertex. As a result, the sampled scenarios partly share the same decision variables. The approach is based on [42,43] and builds upon the SMPC approach that involves a scenario enumeration and a QP proposed by [44].

An illustration of such a tree structure is shown in Fig. 15. Each decision variable  $\Delta\xi^\ell, \ell \in \{1, \dots, L\}$  is associated to a selection of scenarios at the corresponding segment. For example, the value of  $\Delta\xi^{(14)}$  determines by how much the SOC is changing within segment  $i = 4$  for all scenarios  $j \in [59, 100]$ .

We adopt the scenario program (39) dedicated to the classic scenario approach and use an epigraph formulation to simplify the notation and improve the efficiency of finding solutions with appropriate

solvers. As discussed in Section 5.2, a tree structure almost surely calls for an evaluation of the violation probability after solving the problem. Hence, the number of decision variables additionally introduced here is irrelevant. The scenario program for the tree structure then reads as follows:

$$\begin{aligned}
 \min_{\Delta\xi^\ell, E_s^{(i,j)}} & \sum_{j=1}^N \left( \sum_{i=1}^{M_j} E_s^{(i,j)} \right) + \frac{\kappa}{|\mathcal{L}|} \sum_{\ell \in \mathcal{L}} \left( \xi^\ell - \xi_{\text{final}} \right)^2 \\
 \text{s.t.} & \xi^\ell \in \mathbb{X}, \quad \forall \ell = 1, \dots, L, \\
 & E_s^{(i,j)} \geq 0, \quad \forall i = 1, \dots, M_j, j = 1, \dots, N, \\
 & E_s^{(i,j)} \geq \hat{g}^{(i,j)} \left( \Delta\xi^{v(i,j)} \right), \quad \forall i = 1, \dots, M_j, j = 1, \dots, N, \\
 & \Delta\xi^\ell \leq \min_{(i,j) \in S_\ell} \left\{ \overline{\Delta\xi^{(i,j)}} \right\}, \quad \forall \ell = 1, \dots, L,
 \end{aligned} \tag{41}$$

where  $M_j$  is the length of scenario  $j$ ,  $\mathcal{L} \subseteq \{1, \dots, L\}$  is the set of indices representing the leaf vertices, and the cardinality  $|\mathcal{L}|$  denotes the breadth of the tree. To get the vertex for a specific segment  $i$  and scenario  $j$ , we define the function  $\ell = v(i, j)$ . The other way around, the set  $S_\ell$  denotes the pairs of  $(i, j)$  that are associated with the vertex  $\ell$ , i.e.,  $S_\ell = \{(i, j) \in \mathbb{N} \times \mathbb{N} \mid v(i, j) = \ell\}$ . For illustration purposes, we refer to Fig. 15, where  $\mathcal{L} = \{9, 10, 13, 19, 21\}$  and for example  $v(5, 36) = 11$  and  $S_{15} = \{(5, j) \mid j = 59, \dots, 100\}$ . The variable  $\xi^\ell$  denotes the SOC at the vertex  $\ell$  including  $\Delta\xi^\ell$ . It is obtained by adding  $\Delta\xi^\ell$  and all  $\Delta\xi$  values of all ancestors of the vertex  $\ell$  to  $\xi_{\text{init}}$ .

### 5.4. Online learning stochastic model predictive control

The concept of the SCMPC approach proposed in this paper is illustrated in Fig. 16. While in general, the segmentation of the driving missions can be chosen arbitrarily, as discussed in particular in Section 4.3, the SCMPC approach requires a spatially consistent separation of the recorded trips such that the resulting segments can be matched and predictive scenarios can be generated. Motivated by the following case study in Section 6, we exemplarily use bus stops of an urban public transportation system in the following description of the approach as a representation of such separating waypoints.

The controller consists of two processes: The first process represents the learning, prediction, and scenario-based optimization and is triggered whenever the vehicle passes a bus stop. The second process ensures that the power requested by the driver is optimally divided between the battery and the converter and runs at a higher frequency of 1 Hz.

#### 5.4.1. Prediction and optimization

As illustrated in Fig. 16, the purpose of the predictions is to optimize the parameters of the lower-level controller on the basis of a set of scenarios sampled from a database. This database represents the learned road network and consists of data from all previously traveled segments, indexed by the corresponding bus stops at the beginning and end of the segments. The scenarios are generated by sampling sequences of these segments that are linked by the corresponding bus stops. However, in order to prevent unrealistic scenarios such as sudden changes in the direction of travel, we establish a Markov chain (MC) of second order, which provides the probability of an upcoming bus stop as a function of the current and previous ones. The scenarios are then used to formulate a scenario program either with a flat structure (39) or a tree structure (41). The result of the scenario program are sequences of changes of the SOC, which are optimal in the stochastic sense. Obviously, the database must thereby already contain a sufficient number of recorded segments to offer a good enough representation of possible future scenarios.

Since the entire prediction procedure is repeated on a receding horizon whenever the vehicle passes a new bus stop, only the first value

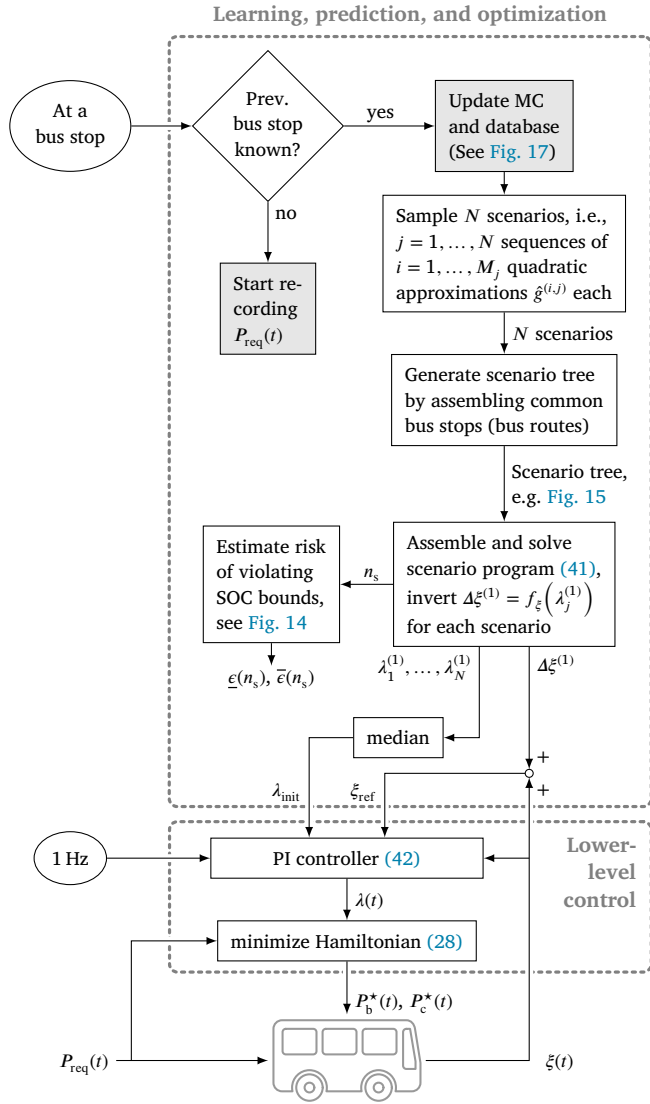


Fig. 16. Flowchart illustrating the SCMPC concept proposed in this paper. Whenever the vehicle passes a bus stop, predictive scenarios are obtained and a scenario program is formulated. Its solution is then used in a lower-level online controller running at a constant frequency of 1 Hz. The blocks highlighted in gray illustrate the learning procedure, which is illustrated in more detail in Fig. 17.

of the result, i.e.,  $\Delta\xi^{(1)}$  is needed. This value can then be used to update the SOC target of an appropriate lower-level controller, such as for example the one proposed in [7]. In addition, we can get an estimate for the ideal value of the costate variable by exploiting again the mappings defined in (33). In particular, by inverting (29), we can find a candidate for the optimal costate value for the first segment of each scenario, denoted by  $\lambda_1^{(1)}, \dots, \lambda_N^{(1)}$ . A reasonable choice for determining representative scalar values is to use average functions or the smallest value, where the latter ensures that the battery is not depleted more than in the worst-case scenario considered. These values may then directly be used to minimize the Hamiltonian function (28) or serve as a feed-forward term for the PI controller, as illustrated in Fig. 16. Finally, based on the number of active constraints and the theoretical bounds on the risk shown in Fig. 14, we can get an estimate of the probability that the SOC bounds are violated in the future.

#### 5.4.2. Learning

The procedure followed to update the database is illustrated in Fig. 17, which is represented by the right block highlighted in gray

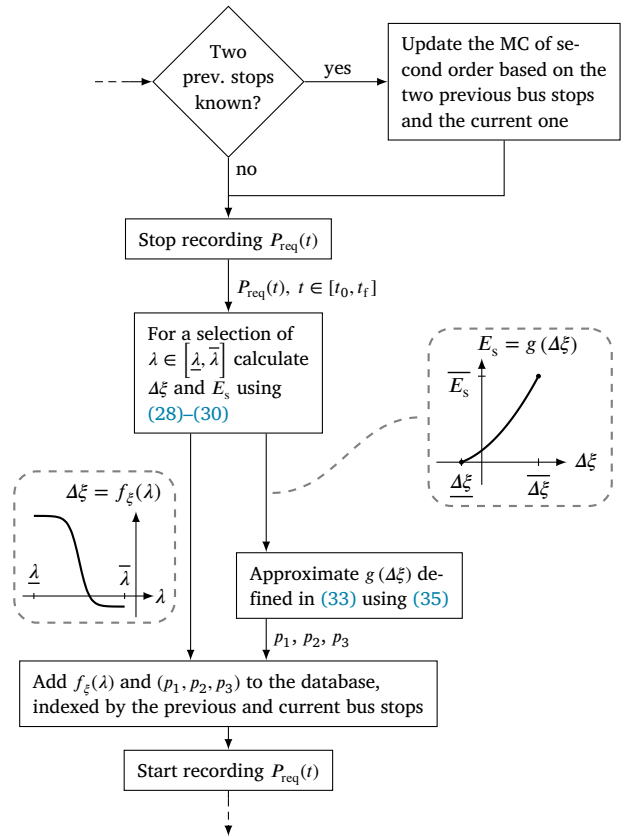


Fig. 17. Flowchart illustrating the procedure followed to update the MC and the database, i.e., the learning process.

in Fig. 16. The power request  $P_{req}(t)$  is continuously recorded while the vehicle is driving between two consecutive bus stops. As soon as the vehicle arrives at a new bus stop, the segment is complete and the recorded trajectory between the start time  $t_0$  and the end time  $t_f$  is processed as follows: First, both the change in SOC and the energy supply are calculated as a function of  $\lambda$  via (29) and (30), respectively. Then, the mapping  $E_s = g(\Delta\xi)$  is created as defined in (33), which is approximated with a quadratic relation as in (35) via the method of least squares. Finally, the resulting set of parameters  $(p_1, p_2, p_3)$  and the function  $\Delta\xi = f_\xi(\lambda)$  are added to the database, indexed by the two bus stops that enclose the segment analyzed.

#### 5.4.3. Lower-level controller

The lower-level controller of the particular setup shown here is implemented as adaptive ECMS (A-ECMS) [45] with the following PI controller for  $\lambda$ :

$$\lambda(t) = \lambda_{init} + K \cdot \left( (\xi(t) - \xi_{ref}) + \frac{1}{T_i} \int_{t_{init}}^t (\xi(\tau) - \xi_{ref}) d\tau \right). \quad (42)$$

Whenever a new solution of the scenario program is available the integrator is reset and both the SOC reference and the initial costate variable  $\lambda_{init}$  are updated. Based on the values of the resulting  $\lambda(t)$  and the current power request  $P_{req}(t)$  we can formulate the Hamiltonian function (26) and minimize it as in (28) to obtain the battery power  $P_b^*(t)$  and the converter power  $P_c^*(t)$ .

## 6. Case study: Battery-assisted trolley bus in Zürich

This section presents a case study that demonstrates the applicability of the proposed SMPC approach. It addresses a trolley bus that is equipped with a battery in order to bridge grid-free sections of the

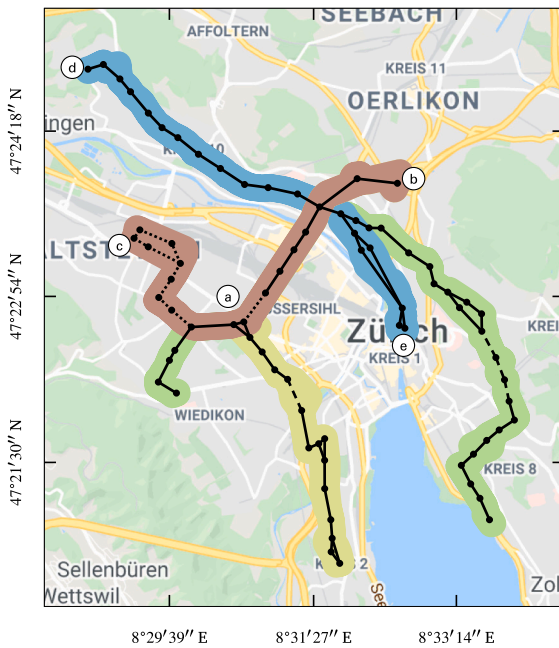


**Fig. 18.** Learned route segments of the trolley bus network in Zürich, superimposed on the four color-coded trolley bus routes, i.e., green: 33, blue: 46, yellow: 72, red: 83. Route 72 resembles Route 83 on the northeastern part. Route 33 resembles Route 83 in its middle part, and follows Route 46 eastwards for a short distance before they separate. The dotted lines indicate grid-free segments. The dashed lines indicate segments which are driven both ways, but are grid-free in only one direction. The circled letters indicate locations visited during the actual test drive. Map data ©2021 Google.

bus routes. The main advantage of not covering the complete routes or removing infrastructure is the reduced total cost of ownership of the public transport operator [46]. In return, the vehicles must be equipped with batteries whose charging strategy is subject to optimization. Obviously, the main goal besides the minimization of energy supply from the grid is to guarantee that the battery never runs out of charge during the grid-free sections, or that in the specific case of the trolley bus under consideration, the SOC never falls below the limit of 50% set by the vehicle control unit.

### 6.1. Setup

The case study presented here is based on four of Zürich's trolley bus routes, the most relevant features of which are listed in Table 3. As all of these bus routes pose different challenges, it is particularly difficult for an online controller to achieve an energy efficient operation without violating the SOC bounds if the bus route is unknown, which is assumed for this case study. We therefore adopt the SMPC concept described in Section 5.4 and illustrated in Figs. 16 and 17, which is able to handle long prediction horizons subject to uncertainty. The vehicle is modeled as described in Sections 2.1.1 and 2.1.2, using the battery, the converter, and the grid parameters listed in Table 1.

To generate predictions, the case study assumes that the MC for predicting the upcoming bus stops and the database have already been generated in a preliminary training step, which covers bus trips of nearly 2800 km over a period of 178 hours on all four bus routes. The corresponding measurements of the power request profiles  $P_{\text{req}}(t)$  are naturally subject to various disturbances, such as climatic conditions, fluctuating auxiliary demands, passenger loads, etc. The resulting learned road network consists of 6548 quadratic approximations distributed among 142 road segments between bus stops, 19 of which are grid-free. The travel distances of these segments are on average 420 m,

**Table 3**

Features of individual round trips of four of Zürich's trolley bus routes.

Route	Duration	Length	Grid-free	Elevation
33	83 min	24.4 km	2.5 km (10.4%)	126 m
46	49 min	14.8 km	0 km (0%)	102 m
72	71 min	18.2 km	1.8 km (9.7%)	72 m
83	59 min	14.7 km	6.1 km (41.2%)	80 m

with a minimum and a maximum of 116 m and 1165 m, respectively. A geographical representation of this database is shown in Fig. 18.

The actual test drive consists of two trips of roughly 97 km in total, with the bus first operating on Route 83 for 3 h and then switching to Route 46 for 3.5 h. The associated elevation profile and the grid availability are shown in the top graph of Fig. 19. The first part of the test drive starts in the depot (a) shown in Fig. 18 and then alternates 2.5 times between the locations (b) and (c), ending again at the depot (a). The second part alternates four times between the locations (d) and (e) after starting at the depot (a), and before ending again at (a).

### 6.2. Online controller

Each time the bus passes a learned road segment a new set of  $N = 100$  independently sampled predictive scenarios is obtained, where each scenario may follow along any route after a junction and consists of as many consecutive segments as necessary for a prediction horizon of 15 km. As mentioned in Section 5.2, a tree structure is preferable when the sampled scenarios are substantially different, which is clearly given here due to the grid-free sections. For example, two scenarios could interfere with each other in a classic formulation if the grid-free sections in the first one are exactly where they are not in the second one, and vice versa. Accordingly, we group the sampled scenarios based on the common stops into a scenario tree, an exemplary result of which is illustrated in Fig. 15, formulate the scenario program (41), and evaluate the probability of violating the SOC constraints a posteriori based on the theoretical bounds shown in Fig. 14.

Based on the resulting optimal change in SOC  $\Delta \xi^{(1)}$  and the corresponding set of costate variable candidates  $\lambda_1^{(1)}, \dots, \lambda_N^{(1)}$  within the first segment, we can update the PI controller parameters as described in Section 5.4.3. Hence,  $\xi_{\text{ref}} = \Delta \xi^{(1)} + \xi(t)$  and  $\lambda_{\text{init}}$  is set to the median of  $\lambda_1^{(1)}, \dots, \lambda_N^{(1)}$ . Before the first scenario program is solved, we use an initial value of  $\lambda_{\text{init}} = -80$  kWh. The controller gain and the time constant are chosen to be  $K = 120$  kWh and  $T_i = 1$  h, respectively. The resulting costate trajectory is shown in the graph second to the bottom of Fig. 19, along with the values of  $\lambda_{\text{init}}$ .

### 6.3. Comparison with other strategies

To compare our approach with other strategies, we simulate the same test drive with a pure A-ECMS controller and with the prescient MPC (P-MPC) strategy, the latter of which assumes perfect knowledge of the future within the prediction horizon. The parameters of the former controller are identical to those of the SCMPC approach mentioned above. They have shown to be a reasonable choice for a variety of driving scenarios on the four trolley bus routes of Zürich. The latter controller is not causal, but allows an estimation of the possible performance with a predictive controller. Its prediction horizon is set to 15 km and its update interval is set to 60 s. In addition, the global optimal benchmark is obtained by solving a TPBVP over the entire horizon of the test drive.

The time-resolved data of Fig. 19 clearly shows that the SCMPC approach maintains a higher SOC than the other strategies, which can be explained by the stochastic predictions that constantly take into account the grid-free sections. Initially, the battery is discharged in the same way as in the A-ECMS. However, as soon as the vehicle is driving on the previously learned road network and the first prediction

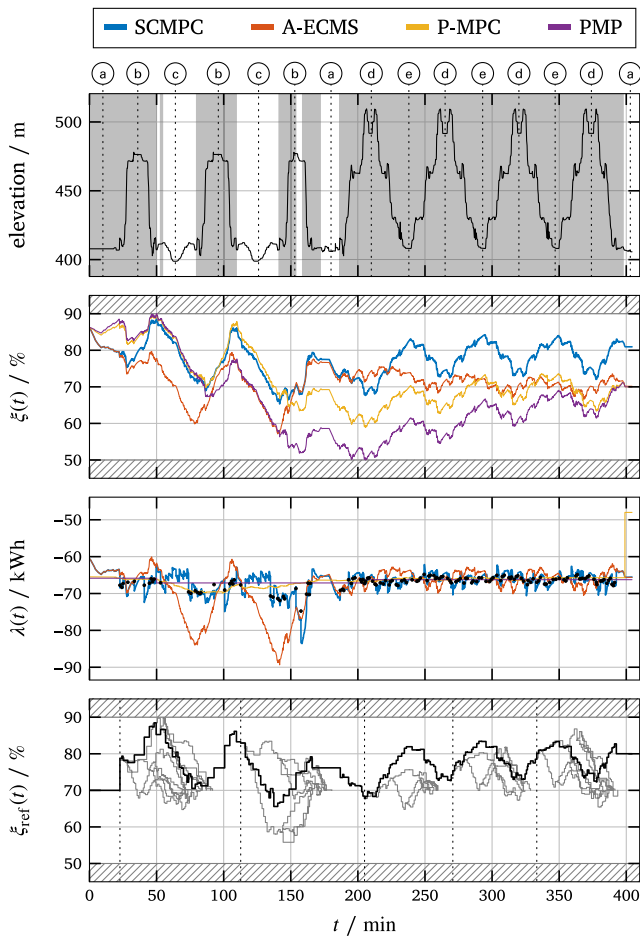


Fig. 19. Time-resolved results of the case study. The top graph shows the elevation profile, superimposed on the grid availability during the test drive in gray. The circled letters together with the dotted lines indicate the times at which the vehicle passes the locations shown in Fig. 18. The color-coded SOC and costate profiles in the middle two graphs allow the results of the proposed SCMPC approach to be compared with the A-ECMS and P-MPC controllers, and to the global optimal benchmark obtained with PMP. The black dots in the graph second to the bottom indicate the values of  $\lambda_{\text{ini}}$ , which are fed forward to the PI controller of the SCMPC approach at the corresponding instances in time. The bottom graph shows the piecewise constant SOC profile  $\xi_{\text{ref}}(t)$  of the SCMPC approach in black and the SOC trajectories  $\xi^{(1)}, \xi^{(2)}, \dots$  of five exemplary scenario trees in gray. The vertically dotted lines indicate the time at which the SOC trajectories are obtained, i.e., the time at which the corresponding scenario program is solved.

Table 4  
Results of the case study.

	$E_s$	$\xi(t_f)$	$E_s - E_f$	$\delta_{\text{PMP}}$
PMP	149.1 kWh	70.0%	1.54 kWh/km	–
P-MPC	149.4 kWh	70.0%	1.54 kWh/km	0.16%
SCMPC	157.8 kWh	80.9%	1.56 kWh/km	1.41%
A-ECMS	152.2 kWh	70.2%	1.57 kWh/km	2.00%

is available, the controller aims to increase the SOC again, resulting in a trajectory almost identical to those of P-MPC and PMP. However, compared to these two strategies, the SCMPC approach maintains a certain SOC margin from the upper bound, evident at about  $t = 50$  min. In the later course from about  $t = 150$  min onwards, the SOC is generally kept higher for more robustness against potential grid-free sections, which ultimately results in a higher final SOC. The bottom graph shows the SOC reference trajectory  $\xi_{\text{ref}}(t)$ , along with five exemplary solutions of the scenario program.

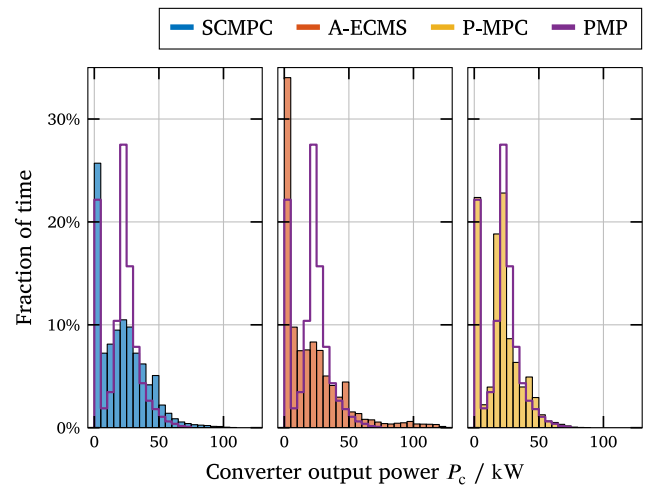


Fig. 20. Histograms of the converter output power  $P_c$  that result from the three online controllers studied, i.e., SCMPC, A-ECMS, and P-MPC, and the global optimal benchmark obtained with PMP. The histogram of the latter is superimposed on the other histograms for comparability.

The numerical results are summarized in Table 4. P-MPC results in the lowest energy consumption among the online controllers and achieves the desired  $\xi_{\text{final}} = 70\%$ . The relative difference in energy supply compared to PMP is only  $\delta_{\text{PMP}} = 0.16\%$ . The two causal controllers SCMPC and A-ECMS both result in a value of  $\xi(t_f)$  that deviates from the desired target. For a numerical comparison, the excessive battery energy  $E_r = (\xi(t_f) - \xi_{\text{final}}) \cdot U_{\text{oc}} Q_0$  is subtracted from the energy supply. This best-case assumption corresponds to lossless charging. Hence, especially the resulting relative error of 1.41% for the SCMPC approach is rather conservative.

The energy savings achieved by the SCMPC approach compared to the A-ECMS can be attributed to the more balanced power distribution over time, shown as histograms in Fig. 20. Due to the greater resistance in the grid compared to the battery and the increase of the grid losses with increasing converter output power  $P_c$ , it is advantageous to aim for low values of  $P_c$  in order to reach the total energy supply required to meet the SOC target. Accordingly, the global optimal benchmark obtained with PMP results in power values that are mostly in a moderate range between 20 kW and 25 kW. While the non-causal controller P-MPC achieves a similar result, the two causal controllers SCMPC and A-ECMS have significantly higher values of  $P_c$ . However, compared to the A-ECMS, the fraction of time  $P_c$  is above 75 kW is significantly reduced by the SCMPC approach, indicating the energy savings achieved.

#### 6.4. Risk evaluation and execution times

During the simulation, 197 scenario programs are solved, on average every 113 s. In only 9 solutions of those, exactly one SOC constraint of (41), i.e.,  $\xi^{(\ell)} \in \mathbb{X}$  is active. The bounds shown in Fig. 14 thus allow the conclusion, that, in general, with high confidence of  $1 - \beta = 99.9\%$ , the SOC constraints are violated with a probability smaller than 10% in roughly 95% of cases and with a probability smaller than 12% in the remaining 5% ones, where a constraint is active. Although we do not have a proof, we expect the violation probability to be lower in practice, since the scenario program is repeatedly solved with new samples whose horizons largely overlap. The number of vertices of the scenario trees, i.e., the number of decision variables, on average amounts to 150, with a minimum of 63 and a maximum of 278.

Concerning the execution times, the transcription and solving of the scenario programs take on average 0.7 s and 1.1 s, respectively. The maximum observed execution times are 1.5 s and 2.8 s, respectively.

The sampling of the scenarios and the construction of the scenario trees can be implemented to be very efficient with a suitable data structure. The simulations presented here are carried out on a laptop computer with an Intel Core i7 processor running at 2.7 GHz and 16 GB of RAM. For solving the convex programs we are using the CasADi [47] interface to Ipopt [48] and the linear solver MUMPS [49]. Given the above execution times and the frequency at which the scenario programs are solved, we conclude that the proposed SCMPC is real-time capable, even with less powerful embedded computers for automotive applications.

## 7. Conclusion

### 7.1. Contribution

In this paper, we propose a new stochastic MPC approach that can take into account long prediction horizons subject to uncertainty, which is particularly relevant for vehicles with large battery capacities. The main contribution is a new technique to combine the optimality conditions of Pontryagin's minimum principle with the scenario approach in order to achieve the computational efficiency that is required for real-time feasible energy management controllers. The approach consists of a division of the driving mission into independent route segments, in each of which the energy supply required to obtain a certain change in the SOC of the battery is described as a quadratic relation. These approximations allow the formulation of convex scenario programs that are capable of taking into account hundreds of scenarios several kilometers long. Moreover, theoretical bounds on the risk of violating the SOC bounds can be applied.

For demonstration purposes, we provide a case study which addresses the energy management of battery-assisted trolley buses equipped with batteries to bridge sections of bus routes where overhead lines are not available. Despite the additional challenge of avoiding to deplete the battery within such grid-free sections with a certain probability, the numerical results of the proposed scenario-based stochastic MPC approach show an increase in the total energy demand of only 1.41% compared the global optimum. Hence, we are convinced of the usefulness of the proposed approach and think that it opens a new perspective in the literature on EMS with uncertain long prediction horizons.

### 7.2. Outlook

In the case study presented, we assume that the bus route is unknown. However, since in practice it is often known, future work could take this information into account when sampling the scenarios. In addition, rare events such as network outages, detours, or unplanned returns to the bus depot could also be considered, although additional caution is needed to ensure that the results are not too conservative. The two validations presented in this paper show that the proposed strategy is applicable not only to battery-assisted trolley buses, but also to other powertrain configurations such as those found in series HEV passenger cars. Further studies could therefore investigate the applicability to such vehicles. Analogously to the grid-free section of trolley buses, emission-free areas could be addressed.

### CRedit authorship contribution statement

**Andreas Ritter:** Conceptualization, Methodology, Software, Formal analysis, Writing – original draft, Visualization. **Fabio Widmer:** Methodology, Software, Writing – review & editing. **Pol Duhr:** Methodology, Writing – review & editing. **Christopher H. Onder:** Conceptualization, Supervision, Project administration, Funding acquisition.

## Declaration of competing interest

The authors declare that they have no known competing financial interests or personal relationships that could have appeared to influence the work reported in this paper.

## Acknowledgments

This work has been supported by the governmental institutions Swiss Federal Office of Energy (SFOE) and Swiss Competence Center for Energy Research (SCCER). The authors would like to thank the industrial partners Carrosserie HESS AG and Verkehrsbetriebe Zürich (VBZ) for realizing the projects providing the data for this study, and Andrea Carron, Marco Weber, and Severin Hänggi for their fruitful discussions.

## Appendix A. Derivation of the Hamiltonian minimization for a battery-assisted trolley bus

The minimization (28) can be carried out algebraically using the battery model (9) and the converter model (13). We assume problem feasibility (18) and in addition (21), such that the power balance  $P_c(t) = P_{\text{req}}(t) - P_b(t)$  is always satisfied. The Hamiltonian function (26) yields

$$H(P_{\text{req}}(t), P_b(t); \lambda) = \frac{U_g}{2 R_g} \left( U_g - \sqrt{U_g^2 - 4 R_g \frac{P_{\text{req}}(t) - P_b(t) + P_0}{e}} \right) - \frac{\lambda}{2 R_b Q_0} \left( U_{\text{oc}} - \sqrt{U_{\text{oc}}^2 - 4 R_b P_b(t)} \right). \quad (\text{A.1})$$

Its derivative w.r.t.  $P_b(t)$  yields

$$\frac{\partial H(\cdot)}{\partial P_b(t)} = - \frac{U_g}{e \sqrt{U_g^2 - 4 \frac{R_g}{e} (P_{\text{req}}(t) - P_b(t) + P_0)}} - \frac{\lambda}{Q_0 \sqrt{U_{\text{oc}}^2 - 4 R_b P_b(t)}}, \quad (\text{A.2})$$

for which the root yields the algebraic solution for the minimum (36).

## Appendix B. Derivation of the Hamiltonian minimization for a series HEV

The minimization (28) using the vehicle-specific converter model (16) can be described using a case distinction and algebraic equations. We assume problem feasibility (18). The optimal battery output power for a given value of  $\lambda$  is

$$P_b(t; \lambda) = \arg \min_{P_b(t)} \left\{ H_{\text{on}}(P_{\text{req}}(t), P_b(t); \lambda), H_{\text{off}}(P_{\text{req}}(t), P_b(t); \lambda) \right\}, \quad (\text{B.1})$$

where the subbranch for the Hamiltonian when the EGU is turned off is given by

$$H_{\text{off}}(P_{\text{req}}(t), P_b(t); \lambda) = \lambda \cdot f_b(P_b(t)). \quad (\text{B.2})$$

Respecting the battery power limits (21), we obtain the optimal battery power and the corresponding Hamiltonian,

$$P_{b,\text{off}}^*(t) = P_{\text{req}}(t), \quad (\text{B.3})$$

$$H_{\text{off}}^*(t; \lambda) = \begin{cases} \lambda \cdot f_b(P_{b,\text{off}}^*(t); \lambda) & \text{if } P_{\text{req}}(t) \leq \widehat{P}_b, \\ \infty & \text{otherwise,} \end{cases} \quad (\text{B.4})$$

where the latter case ensures that the EGU is used if the power request exceeds the battery power limits. If the EGU is running, the subbranch for the Hamiltonian yields

$$H_{\text{on}}(P_{\text{req}}(t), P_b(t); \lambda) = \alpha_1 (P_{\text{req}}(t) - P_b(t))^2 + \alpha_2 (P_{\text{req}}(t) - P_b(t)) + \alpha_3 + \lambda \cdot f_b(P_b(t)), \quad (\text{B.5})$$

for which the first and second derivatives w.r.t.  $P_b(t)$  yield

$$\frac{\partial H_{\text{on}}}{\partial P_b} = -2\alpha_1 (P_{\text{req}} - P_b) - \alpha_2 - \frac{\lambda}{Q_0 \sqrt{U_{\text{oc}}^2 - 4 R_b P_b}}, \quad (\text{B.6})$$

$$\frac{\partial^2 H_{\text{on}}}{\partial P_b^2} = 2\alpha_1 - 2 \frac{\lambda R_b}{Q_0 (U_{\text{oc}}^2 - 4 R_b P_b)^{3/2}}, \quad (\text{B.7})$$

respectively, where all time and variable dependencies were omitted for clarity. An algebraic solution for the minimum can be derived via the roots of (B.6). Moreover, from (B.7) being greater than zero for all  $\lambda \leq 0$  and  $P_b(t) < U_{\text{oc}}^2/4 R_b$ , we know that (B.5) is convex and has a unique minimizer.

The roots of (B.6) can be expressed via the cubic equation

$$a P_b(t)^3 + b(t) P_b(t)^2 + c(t) P_b(t) + d(t) = 0, \quad (\text{B.8})$$

for the derivation of which both sides of the equation are squared. The extraneous solutions introduced by this step can be discarded a posteriori by validating that (B.6) is equal to zero. The coefficients are

$$\begin{aligned} a &= -16 \alpha_1^2 R_b, \\ b &= 4 \alpha_1^2 U_{\text{oc}}^2 - 2 a P_{\text{req}} + 16 \alpha_1 \alpha_2 R_b, \\ c &= 4 \alpha_1 \alpha_2 (4 R_b P_{\text{req}} - U_{\text{oc}}^2) - 4 \alpha_2^2 R_b - 2 b P_{\text{req}} - 3 a P_{\text{req}}^2, \\ d &= 4 \alpha_1^2 U_{\text{oc}}^2 P_{\text{req}}^2 + 4 \alpha_1 \alpha_2 U_{\text{oc}}^2 P_{\text{req}} + \alpha_2^2 U_{\text{oc}}^2 - \lambda^2 / Q_0^2, \end{aligned} \quad (\text{B.9})$$

where all time dependencies were omitted for clarity. Using the primitive cube root of unity,  $z = -\frac{1}{2} + \frac{\sqrt{-3}}{2}$ , and the following auxiliary variables defined via the coefficients of (B.9),

$$\begin{aligned} \varphi &= 2b^3 - 9abc + 27a^2d, \\ \phi &= b^2 - 3ac, \\ \psi &= \sqrt[3]{\frac{1}{2}(\varphi - \sqrt{\varphi^2 - 4\phi^3})}, \end{aligned} \quad (\text{B.10})$$

the three candidates for the minimizer are given by

$$P_{b,\text{on}}^{(k)}(t; \lambda) = -\frac{1}{3a} \left( b + \psi z^k + \frac{\phi}{\psi z^k} \right), \quad k = \{0, 1, 2\} \quad (\text{B.11})$$

Plugging (B.11) into (B.6) reveals the correct minimizer  $P_{b,\text{on}}(t; \lambda)$  for (B.5). Respecting the battery power limits, we obtain

$$P_{b,\text{on}}^*(t; \lambda) = \max \left\{ P_b, \min \left\{ P_{b,\text{on}}(t; \lambda), \widehat{P}_b \right\} \right\}, \quad (\text{B.12})$$

$$H_{\text{on}}^*(t; \lambda) = H_{\text{on}}(P_{\text{req}}(t), P_{b,\text{on}}^*(t; \lambda)). \quad (\text{B.13})$$

Finally, we obtain the optimal battery power as follows:

$$P_b^*(t; \lambda) = \begin{cases} P_{b,\text{off}}^*(t; \lambda) & \text{if } H_{\text{off}}^*(t; \lambda) \leq H_{\text{on}}^*(t; \lambda) \\ P_{b,\text{on}}^*(t; \lambda) & \text{otherwise.} \end{cases} \quad (\text{B.14})$$

## References

[1] European Environment Agency. Greenhouse gas emissions from transport in Europe. 2020, <https://www.eea.europa.eu/data-and-maps/indicators/transport-emissions-of-greenhouse-gases-7/assessment>. [Accessed 20 March 2021].

[2] European Commission. The European green deal. COM(2019) 640 final. 2019, Communication from the Commission to the European Parliament, the European Council, the Council, the European Economic and Social Committee and the Committee of the Regions, Brussels.

[3] Melliger MA, van Vliet OP, Liimatainen H. Anxiety vs. reality – Sufficiency of battery electric vehicle range in Switzerland and Finland. *Transp Res D: Transp Environ* 2018;65:101–15. <http://dx.doi.org/10.1016/j.trd.2018.08.011>.

[4] Paganelli G, Ercole G, Brahma A, Guezennec Y, Rizzoni G. General supervisory control policy for the energy optimization of charge-sustaining hybrid electric vehicles. *JSAE Rev* 2001;22(4):511–8. [http://dx.doi.org/10.1016/S0389-4304\(01\)00138-2](http://dx.doi.org/10.1016/S0389-4304(01)00138-2).

[5] Paganelli G, Delprat S, Guerra TM, Rimaux J, Santin JJ. Equivalent consumption minimization strategy for parallel hybrid powertrains. In: Vehicular technology conference. IEEE 55th vehicular technology conference. VTC spring 2002 (Cat. No.02CH37367), vol. 4. 2002, p. 2076–81. <http://dx.doi.org/10.1109/VTC.2002.1002989>.

[6] Serrao L, Onori S, Rizzoni G. ECMS as a realization of Pontryagin's minimum principle for HEV control. In: 2009 American control conference. 2009, p. 3964–9. <http://dx.doi.org/10.1109/ACC.2009.5160628>.

[7] Ambühl D, Guzzella L. Predictive reference signal generator for hybrid electric vehicles. *IEEE Trans Veh Technol* 2009;58(9):4730–40. <http://dx.doi.org/10.1109/TVT.2009.2027709>.

[8] Tianheng F, Lin Y, Qing G, Yanqing H, Ting Y, Bin Y. A supervisory control strategy for plug-in hybrid electric vehicles based on energy demand prediction and route preview. *IEEE Trans Veh Technol* 2015;64(5):1691–700. <http://dx.doi.org/10.1109/TVT.2014.2336378>.

[9] Zhang C, Vahidi A, Pisu P, Li X, Tennant K. Role of terrain preview in energy management of hybrid electric vehicles. *IEEE Trans Veh Technol* 2010;59(3):1139–47. <http://dx.doi.org/10.1109/TVT.2009.2038707>.

[10] Xie S, Hu X, Xin Z, Brighton J. Pontryagin's minimum principle based model predictive control of energy management for a plug-in hybrid electric bus. *Appl Energy* 2019;236:893–905. <http://dx.doi.org/10.1016/j.apenergy.2018.12.032>.

[11] Pei D, Leamy MJ. Dynamic programming-informed equivalent cost minimization control strategies for hybrid-electric vehicles. *J Dyn Syst Meas Control* 2013;135(5). <http://dx.doi.org/10.1115/1.4024788>.

[12] Koot M, Kessels JTBA, de Jager B, Heemels WPMH, van den Bosch PPJ, Steinbuch M. Energy management strategies for vehicular electric power systems. *IEEE Trans Veh Technol* 2005;54(3):771–82. <http://dx.doi.org/10.1109/TVT.2005.847211>.

[13] Johannesson L, Murgovski N, Jonasson E, Hellgren J, Egardt B. Predictive energy management of hybrid long-haul trucks. *Control Eng Pract* 2015;41:83–97. <http://dx.doi.org/10.1016/j.conengprac.2015.04.014>.

[14] Buerger J, Cannon M. Nonlinear MPC for supervisory control of hybrid electric vehicles. In: 2016 European control conference. 2016, p. 135–40. <http://dx.doi.org/10.1109/ECC.2016.7810276>.

[15] Bertsekas DP. Dynamic programming and optimal control, vol. 1. 3rd ed.. Belmont, MA, USA: Athena Scientific; 2005.

[16] Kolmanovsky I, Siverguina I, Lygoe B. Optimization of powertrain operating policy for feasibility assessment and calibration: Stochastic dynamic programming approach. In: Proceedings of the 2002 American control conference (IEEE Cat. No.CH37301), vol. 2. 2002, p. 1425–30 vol.2. <http://dx.doi.org/10.1109/ACC.2002.1023221>.

[17] Johannesson L, Asbogard M, Egardt B. Assessing the potential of predictive control for hybrid vehicle powertrains using stochastic dynamic programming. *IEEE Trans Intell Transp Syst* 2007;8(1):71–83. <http://dx.doi.org/10.1109/ITITS.2006.884887>.

[18] Bellman R. Dynamic programming. Mineola, NY, USA: Dover Publications, Inc.; 2003.

[19] Farina M, Giulioni L, Scattolini R. Stochastic linear model predictive control with chance constraints – A review. *J Process Control* 2016;44:53–67. <http://dx.doi.org/10.1016/j.jprocont.2016.03.005>.

[20] Wulf Ribelles L, Padilla G, Donkers M. Traffic-aware vehicle energy management strategies via scenario-based optimization. *IFAC-PapersOnLine* 2020;53(2):14217–23. <http://dx.doi.org/10.1016/j.ifacol.2020.12.1065>, 21th IFAC World Congress.

[21] Di Cairano S, Bernardini D, Bemporad A, Kolmanovsky IV. Stochastic MPC with learning for driver-predictive vehicle control and its application to HEV energy management. *IEEE Trans Control Syst Technol* 2014;22(3):1018–31. <http://dx.doi.org/10.1109/TCST.2013.2272179>.

[22] Liu B, Wang Y. Energy system optimization under uncertainties: A comprehensive review. In: Ren J, Wang Y, He C, editors. Towards sustainable chemical processes. Elsevier; 2020, p. 149–70. <http://dx.doi.org/10.1016/b978-0-12-818376-2.00006-5>.

[23] Guzzella L, Sciarretta A. Vehicle propulsion systems: Introduction to modeling and optimization. 3rd ed. 2013.. Berlin, Heidelberg: Springer Berlin Heidelberg; 2013. <http://dx.doi.org/10.1007/978-3-642-35913-2>.

[24] Sciarretta A, Guzzella L. Control of hybrid electric vehicles. *IEEE Control Syst Mag* 2007;27(2):60–70. <http://dx.doi.org/10.1109/MCS.2007.338280>.

[25] Elbert P, Nüesch T, Ritter A, Murgovski N, Guzzella L. Engine On/Off control for the energy management of a serial hybrid electric bus via convex optimization. *IEEE Trans Veh Technol* 2014;63(8):3549–59. <http://dx.doi.org/10.1109/TVT.2014.2304137>.

- [26] Schildbach G, Fagiano L, Frei C, Morari M. The scenario approach for stochastic model predictive control with bounds on closed-loop constraint violations. *Automatica* 2014;50(12):3009–18. <http://dx.doi.org/10.1016/j.automatica.2014.10.035>.
- [27] Campi MC, Garatti S. Introduction to the scenario approach. Philadelphia, PA: Society for Industrial and Applied Mathematics; 2018. <http://dx.doi.org/10.1137/1.9781611975444>.
- [28] Pontryagin LS. In: Boltyanskii VG, Mishchenko EF, Gamkrelidze RV, Tiriogoff KN, Neustadt LW, Pontryagin LS, editors. The mathematical theory of optimal processes. L.S. Pontryagin selected works, 1. vol. 4, London: Routledge; 2018. <http://dx.doi.org/10.1201/9780203749319>.
- [29] de Jager B, van Keulen T, Kessels J. Optimal control of hybrid vehicles. *Advances in industrial control*, London: Springer; 2013. <http://dx.doi.org/10.1007/978-1-4471-5076-3>.
- [30] Kutter S, Bäker B. An iterative algorithm for the global optimal predictive control of hybrid electric vehicles. In: 2011 IEEE vehicle power and propulsion conference. 2011, p. 1–6. <http://dx.doi.org/10.1109/VPPC.2011.6043004>.
- [31] van Keulen T, Gillot J, de Jager B, Steinbuch M. Solution for state constrained optimal control problems applied to power split control for hybrid vehicles. *Automatica* 2014;50(1):187–92. <http://dx.doi.org/10.1016/j.automatica.2013.09.039>.
- [32] Wei X, Guzzella L, Utkin VI, Rizzoni G. Model-based fuel optimal control of hybrid electric vehicle using variable structure control systems. *J Dyn Syst Meas Control* 2006;129(1):13–9. <http://dx.doi.org/10.1115/1.2397148>.
- [33] Delprat S, Hofman T, Paganelli S. Hybrid vehicle energy management: Singular optimal control. *IEEE Trans Veh Technol* 2017;66(11):9654–66. <http://dx.doi.org/10.1109/TVT.2017.2746181>.
- [34] Sager S. Numerical methods for mixed-integer optimal control problems (Ph.D. thesis), Heidelberg, Germany: Universität Heidelberg; 2006.
- [35] Boyd S, Vandenberghe L. *Convex optimization*. Cambridge, UK: Cambridge University Press; 2004.
- [36] Schildbach G, Fagiano L, Morari M. Randomized solutions to convex programs with multiple chance constraints. *SIAM J Optim* 2013;23(4):2479–501. <http://dx.doi.org/10.1137/120878719>.
- [37] Campi MC, Garatti S. A sampling-and-discarding approach to chance-constrained optimization: Feasibility and optimality. *J Optim Theory Appl* 2011;148(2):257–80. <http://dx.doi.org/10.1007/s10957-010-9754-6>.
- [38] Zhang X, Grammatico S, Schildbach G, Goulart P, Lygeros J. On the sample size of random convex programs with structured dependence on the uncertainty. *Automatica* 2015;60:182–8. <http://dx.doi.org/10.1016/j.automatica.2015.07.013>.
- [39] Campi MC, Garatti S. Wait-and-judge scenario optimization. *Math Program* 2018;167(1):155–89. <http://dx.doi.org/10.1007/s10107-016-1056-9>.
- [40] Garatti S, Campi MC. Risk and complexity in scenario optimization. *Math Program* 2019;1–37. <http://dx.doi.org/10.1007/s10107-019-01446-4>.
- [41] Carè A, Garatti S, Campi MC. The wait-and-judge scenario approach applied to antenna array design. *Comput Manag Sci* 2019;16(3):481–99. <http://dx.doi.org/10.1007/s10287-019-00345-5>.
- [42] Ripaccioli G, Bernardini D, Di Cairano S, Bemporad A, Kolmanovskiy IV. A stochastic model predictive control approach for series hybrid electric vehicle power management. In: Proceedings of the 2010 American control conference. 2010, p. 5844–9. <http://dx.doi.org/10.1109/ACC.2010.5530504>.
- [43] Bichi M, Ripaccioli G, Di Cairano S, Bernardini D, Bemporad A, Kolmanovskiy IV. Stochastic model predictive control with driver behavior learning for improved powertrain control. In: 49th IEEE conference on decision and control. 2010, p. 6077–82. <http://dx.doi.org/10.1109/CDC.2010.5717791>.
- [44] Bernardini D, Bemporad A. Stabilizing model predictive control of stochastic constrained linear systems. *IEEE Trans Automat Control* 2012;57(6):1468–80. <http://dx.doi.org/10.1109/TAC.2011.2176429>.
- [45] Musardo C, Rizzoni G, Staccia B. A-ECMS: An adaptive algorithm for hybrid electric vehicle energy management. In: Proceedings of the 44th IEEE conference on decision and control. 2005, p. 1816–23. <http://dx.doi.org/10.1109/CDC.2005.1582424>.
- [46] Meishner F, Sauer DU. Technical and economic comparison of different electric bus concepts based on actual demonstrations in European cities. *IET Electr Syst Transp* 2020;10(2):144–53. <http://dx.doi.org/10.1049/iet-est.2019.0014>.
- [47] Andersson JAE, Gillis J, Horn G, Rawlings JB, Diehl M. CasADi – A software framework for nonlinear optimization and optimal control. *Math Program Comput* 2019;11(1):1–36. <http://dx.doi.org/10.1007/s12532-018-0139-4>.
- [48] Wächter A, Biegler LT. On the implementation of an interior-point filter line-search algorithm for large-scale nonlinear programming. *Math Program* 2006;106(1):25–57. <http://dx.doi.org/10.1007/s10107-004-0559-y>.
- [49] Padua D, editor. *MUMPS*. In: Encyclopedia of parallel computing. Boston, MA: Springer US; 2011, p. 1238. [http://dx.doi.org/10.1007/978-0-387-09766-4\\_2260](http://dx.doi.org/10.1007/978-0-387-09766-4_2260).